

Strain effects in low-dimensional transition metal oxides

Jinbo Cao^{a,b,*}, Junqiao Wu^{a,b}

^a Department of Materials Science and Engineering, University of California, Berkeley, CA 94720, United States

^b Materials Sciences Division, Lawrence Berkeley National Laboratory, Berkeley, CA 94720, United States

ARTICLE INFO

Keywords:

Nanowire
Thin film
Strain
Transition metal oxide
Correlated electron material
Phase transition

ABSTRACT

Transition metal oxides offer a wide spectrum of properties which provide the foundation for a broad range of potential applications. Many of these properties originate from intrinsic coupling between lattice deformation and nanoscale electronic and magnetic ordering. Lattice strain thus has a profound influence on the electrical, optical, and magnetic properties of these materials. Recent advances in materials processing have led to the synthesis of low-dimensional single-crystal transition metal oxides, namely, epitaxial ultra-thin films and free-standing nano/microwires. Unlike bulk materials, these systems allow external tuning of uniform strain in these materials to tailor their properties and functionalities.

This paper provides a comprehensive review of recent developments in studies of strain effects in transition metal oxide ultra-thin films and nano/microwires. In epitaxial thin films, biaxial strain is developed as a result of lattice mismatch between the film and the substrate. By choosing different substrates, a wide range of strain can be established at discrete values that allows for exploration of new phase space, enhancement of order parameters, creation of complicated domain textures, and stabilization of new phases. On the other hand, continuous tuning of uniaxial strain is possible in nano/microwires, where a variety of phase transitions and their dynamics could be probed at the single or few-domain scale. We focus on the work of strain-controlled electromechanical response in piezoelectric oxides and strain-induced metal–insulator transitions as well as domain physics in strongly correlated electron oxides. Related nanoscale device applications such as strain sensing and power generation will be highlighted as well.

Published by Elsevier B.V.

Contents

1. Introduction	36
1.1. Spin–lattice–charge coupling in transition metal oxides	36
1.2. Epitaxial growth of TMO thin films	36
1.3. Synthesis of free-standing TMO nanowires	37
2. Strain effects in TMO thin films	38
2.1. Ferroelectric thin films	38
2.1.1. Theoretical and experimental characterization	38
2.1.2. Results of specific materials	39
2.2. Magnetoresistive manganese perovskites	42
2.2.1. Phase separation and domain pattern	42
2.2.2. Effects on transport properties	42
3. Strain effects in TMO micro/nanowires	45
3.1. Electromechanics in TMO micro/nanowires	45
3.2. Phase transitions and domain physics under strain	45
3.2.1. Phase inhomogeneity and domain organization	45
3.2.2. Investigation of phase transition at the single-domain level	46
3.2.3. Superelasticity in phase transition	47
3.2.4. Domain dynamics and manipulation	47
3.2.5. New phase stabilization with strain	49

* Corresponding author at: Department of Materials Science and Engineering, University of California, Berkeley, CA 94720, United States.
E-mail address: jcao@lbl.gov (J. Cao).

4. New opportunities for applications	49
5. Conclusions and outlook	50
Acknowledgements	50
References	50

1. Introduction

1.1. Spin–lattice–charge coupling in transition metal oxides

Transition metal oxides (TMOs) exhibit rich and fascinating properties including piezo/ferroelectricity, high- T_C superconductivity, colossal magnetoresistance, and nonlinear optical behavior, and these properties can be tailored for a wide variety of emergent applications [1]. Most of these remarkable properties originate from the interplay between spin, lattice, charge, and orbital degrees of freedom of the material [1,2]. These competing factors typically result in complicated phase diagrams and render their properties highly sensitive to a variety of chemical and physical perturbations [3]. Lattice strain is such an external stimulus that can be employed to control and drastically engineer the properties of TMOs. In contrast to conventional metals and semiconductors where elastic strain causes only non-disruptive effects [4,5], strain has profound influence on the electrical, optical, and magnetic properties of TMOs through intrinsic coupling between charge, spin and orbital wavefunctions of electrons. Fig. 1 shows a schematic view of the electromechanics of TMOs, where the direct and indirect effects of stress and strain on TMOs can be seen. Control and engineering of strain have become an important strategy for achieving novel functionalities and probing exotic properties of TMOs.

It is well known that the physical properties of electric and magnetic materials can be modified by application of hydrostatic pressure [6,7]. However, bulk inorganic materials can only sustain extremely low non-hydrostatic strain (typically < 0.1%) before plastic deformation or fracture occurs. Recent advances in growth of thin films and nanowires of TMOs present possibility of applying extraordinarily large and non-hydrostatic stress benefiting from the smaller number of structural defects in these low-dimensional systems compared to their bulk counterparts. For sufficiently thin films, biaxial strain of several percent can be achieved by growing the layer on lattice-mismatched substrates. Such biaxial strain was used to increase the transition temperature in high- T_C superconductors [8–10] and ferroelectric materials [11–13]. Other parameters such as saturation magnetization in ferromagnets [14,15] and spontaneous polarization in ferroelectrics are also strongly affected by strain [13,16]. Here the biaxial strain is imposed to the epilayer through the lattice mismatch with the

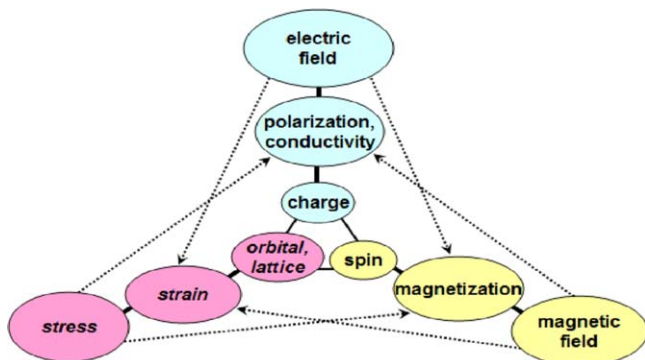


Fig. 1. Electromechanics of TMOs: stress influences electronic and magnetic properties through intrinsic coupling between the charge, spin and orbital degrees of freedom of electrons.

underlying substrate. The strain distribution might be complicated by misfit dislocations that can partially relax the strain and cause structural and physical inhomogeneities in the films. To circumvent this problem, fully coherent strained (pseudomorphic), epitaxial films were grown below the critical thickness. By growing such ultra-thin layers on atomically smooth substrates, dislocation can be avoided so that the intrinsic effect of strain of TMOs can be extracted. Alternatively, it is also possible to study the strain effect by stressing free-standing nanoscale TMOs. As these materials are typically single crystals and dislocation-free, they can sustain an extraordinary amount of uniaxial strain without fracturing and the strain is also continuously tunable by varying the external stress.

Our review is focused on recent developments in studies of strain effects in pseudomorphic thin films and micro/nano scale wires of TMOs. For TMO thin films we will focus on ferroelectrics and colossal magnetoresistive manganites. On the other hand, for the continuous tuning of strain in free-standing TMOs, we will focus on energy scavenging using piezoelectric materials BaTiO₃ and ZnO, and domain organization and manipulation in VO₂ wires. After a brief summary of standard techniques to grow high-quality thin films and micro/nanowires, we will describe how strain is employed to explore the phase space, enhance order parameters, create complicated domain textures, and stabilize new phases in TMOs. Theoretical models and predictions will be discussed along with experiments. Related nanoscale device applications such as strain sensing and power generation will also be discussed.

1.2. Epitaxial growth of TMO thin films

Growth of strained oxide thin films predominantly relies on heteroepitaxy, where a single-crystalline film with specific orientation is deposited on the atomically smooth surface of the substrate. These two materials typically share similar interfacial structure, therefore the structure and crystal orientation of the epilayer are determined by the structure and surface plane of the substrate. By carefully choosing the substrate and growth conditions, coherently strained epitaxial films with homogeneous biaxial strain can be grown with few or no misfit dislocations. Strain can also be induced to the films through different thermal expansion between the film and the underlying substrate, or extended defects formed during film deposition. However, residual stress incorporated in these two methods is typically complicated, making it difficult to investigate the intrinsic effect of strain on material properties [17–19].

Physical vapor deposition (PVD) and chemical vapor deposition (CVD) are the most common methods for deposition of TMO thin films [20,21]. They prove to be reliable ways to transfer materials atom by atom from one or more sources to the growth surface. The deposition is normally carried out at high background vacuum so that the vapor composition can be well controlled. During the PVD, physical processes such as sputtering and evaporation are employed to deposit films. In the sputtering deposition, atoms are ejected from a solid target by the bombardment of the target materials with energetic ions. Many different sputtering methods such as DC sputtering, radio frequency sputtering, and magnetron sputtering are widely used for the deposition of TMO thin films [22–24]. Molecular beam epitaxy (MBE) is an example of the evaporation method. In MBE,

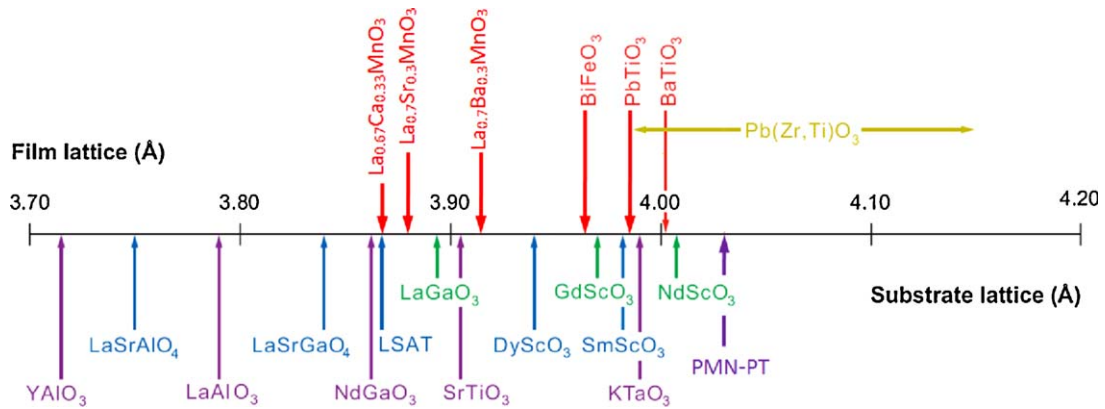


Fig. 2. A number line showing the pseudotetragonal or pseudocubic a -axis lattice parameters of commercial substrates (below the number line) [35] and perovskite ABO_3 thin films of interest in this review (above the number line). The numbers for perovskite films represent the lattice constants of unstrained film or bulk samples [35].

the solid targets are heated until they begin to emit gaseous atoms. The atomic beam travels to the substrate and then condenses there to form thin films. The most important aspect of MBE is the slow deposition rate, which allows the films to grow epitaxially, with atomically controlled thickness and composition [11,13,25–27]. Pulsed laser deposition (PLD) is a method where a high-power pulsed laser beam is used to ablate a target and vaporize the materials (in a plasma plume), which is subsequently deposited as a thin film on the substrate. The whole process of PLD is rather complicated, including the laser induced evaporation, ablation, and plasma formation. Typically a large supersaturation exists on the substrate during the laser pulse. This high supersaturation causes a very large nucleation density on the surface compared to MBE or sputtering deposition and therefore results smoother thin films [28–31]. Chemical vapor deposition differs from PVD in that a chemical process is involved during the deposition process. Volatile precursors are used in the process and they react on the hot surface of the substrate to form thin films. Metal-organic chemical vapor deposition (MOCVD) has been utilized successfully for the deposition of oxide films such as high- T_C superconductors and ferroelectrics [32–34].

Both PVD and CVD can be employed to grow crystalline phase and even epitaxial films on nearly lattice-matched substrates. The quality of the underlying substrate is very important for this purpose. The availability of appropriate substrates and methods to prepare smooth and defect-free surfaces for epitaxial growth of TMOs is crucial. A lot of perovskite-related single-crystal substrates with structural perfection comparable to that of single-crystal semiconductors are commercially available and are well suited for epitaxial growth of perovskite-compatible thin films. These single-crystal substrates include $YAIO_3$, $LaAlO_3$, $LaSrGaO_4$, $NdGaO_3$, $SrTiO_3$, $DyScO_3$, etc. [35]. It is fortunate that many functional TMOs including ferroelectric titanites, colossal magnetoresistive manganites, and high- T_C superconductor cuprates have perovskite or perovskite-derived structures. As shown in Fig. 2, the lattice parameters of these functional TMOs are very close to those of available substrates. By growing perovskite thin films on the substrates, the epitaxial layer will be similar to the substrates in lattice constants and therefore will be naturally strained if the lattice parameters between the film and substrate are slightly different. Here the biaxial strain is defined as $\varepsilon = (a_{\text{film}} - a_{\text{bulk}})/a_{\text{bulk}}$. Note that a progressive relaxation might occur throughout the film thickness, and the measured lattice constants a_{film} can be different from that of the underlying substrate. In any case, epitaxial growth of thin films on substrates provides an efficient and effective way to manipulate and control strain in TMOs.

1.3. Synthesis of free-standing TMO nanowires

TMO nanowires can be synthesized in numerous ways including top-down and bottom-up processes [36]. Bottom-up processes involve chemical synthesis and/or highly controlled deposition and growth of materials. According to the synthesis environment, they can be roughly classified into vapor-phase growth and liquid phase growth. The vapor-phase technique is based on the reaction between metal vapor and oxygen gas, and has been successfully employed to synthesize many metal oxide nanostructures. The governing mechanisms during the vapor-phase growth are the vapor–liquid–solid process or vapor–solid process. The simplest vapor-phase growth technique involves a thermal furnace where metal vapor source and oxygen gas can react in a controlled way. The aforementioned techniques such as PLD and MOCVD that are widely used in thin-film growth have been exploited to best control the morphology and crystallinity of the synthesized nanomaterials [37,38]. Fig. 3 shows a schematic view of a typical thermal vapor transport setup. A horizontal quartz tube with gas flowing inside is placed in a heating furnace. The growth substrate is placed downstream of the source for the nanostructure growth. During the vapor-phase growth, high temperature is typically used to vaporize the solid source. The vapor will then be transported by the carrier gas and deposited on the substrate through simple condensation or with chemical reactions. Nanoparticle catalysts are typically used to guide the growth of nanowires, although in some cases it is also possible to grow TMOs without catalysts [39–41]. On the other hand, solution-phase growth methods provide more flexible synthesis and the nanostructured materials can be synthesized at more benign environments. To develop strategies that can guide and confine the growth direction to form TMO nanowires, researchers have used template-assisted synthesis, sol-gel deposition, surfactant-

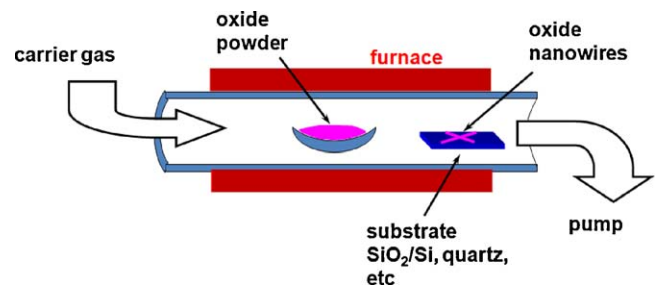


Fig. 3. Schematic view of vapor transport synthesis that can be used in CVD, PVD, and PLD to grow TMO nanowires.

assisted growth, molten-salt method, and hydrothermal growth. There have been many reviews for growing oxide nanowires [36,42]. The effects of strain on BaTiO₃, ZnO, and VO₂ nanowires have been extensively investigated in literature and will be the focus of our review. These TMO nanowires were grown via vapor transport or molten-salt methods [40,43,44].

2. Strain effects in TMO thin films

2.1. Ferroelectric thin films

2.1.1. Theoretical and experimental characterization

Ferroelectrics are a family of materials that behave as normal dielectrics at high temperatures, but possess a permanent electric dipole moment when they are cooled below the ferroelectric transition temperatures (i.e., Curie temperature, T_C). The polarization mechanism is typically the spontaneous displacement of ionic charges within the unit cell. Most common ferroelectrics are TMOs, such as PbTiO₃, BaTiO₃, Pb(Zr_xTi_{1-x})O₃, BiFeO₃, etc. One of the common features for ferroelectric crystals is the formation of domain structures when they pass through the Curie temperature and transform into the ferroelectric phase, as typically multiple degenerate states with different polarization directions exist in the ferroelectric phase. All ferroelectric phase transitions are accompanied by a change in the unit cell and the crystal structures. The domain configuration therefore responds to external stress. Effects of microstresses on the thermodynamics of polydomains were well studied [45]. When ferroelectric thin films are grown on a substrate, the domain pattern, Curie temperature, and spontaneous polarization can be significantly affected by the substrate-induced strain. (see, e.g., recent reviews [35,46–48])

In order to understand and model the strain effect of ferroelectric thin films, many methods including first-principles calculations [49–53], molecular dynamics simulations [54,55], phenomenological Landau–Devonshire analysis [56–59], and phase-field models [46,60,61] have been applied. Among the calculations, a free energy function is first identified and then minimized with respect to various independent degrees of freedom to predict the state as a function of strain, temperature, and macroscopic electric field. The energy functions can be obtained from first-principle calculations or phenomenological methods such as Landau–Devonshire expansion. First-principle calculations have the advantages of predicting the exact atomic arrangements and polarization-related properties without input of experimental information. With the help of density functional perturbation theory, development of new algorithms, and increasing computational powers, nowadays it is possible for first-principle calculations to handle supercells that contain hundreds of atoms [49,62]. For example, recently first-principle computations were used to map out the structural instabilities in the Ruddlesden–Popper homologous oxide superlattices, and demonstrate that competition between different instabilities can be greatly influenced by epitaxial strain [50]. Phenomenological approaches can reach macroscopic continuum scales and provide accurate analysis of materials on the practical experimental scale [58,59]. In addition, by choosing appropriate general functions for multiple-domain or multiphase states, phase-field analysis can predict the domain structures and properties of ferroelectric thin films as a function of temperature, substrate constraints, thickness, and electrical boundary conditions [46,61,63,64].

There are many experimental techniques that can characterize the properties of strained ferroelectric thin films. For example, transmission electron microscopy (TEM) has been widely used to image interface structures and extended defects in thin films [67–69]. As the ferroelectric transition of a material is always accompanied by a structural change, and all the ferroelectrics

must lack inversion symmetry, methods that provide direct information on local structures can therefore be used to probe ferroelectricity. From general theoretical considerations, changes in the ferroelectric order parameter are expected near interfaces. It is important to determine how the polarization and corresponding atomic structure vary in the proximity of ferroelectric interfaces, especially in ultra-thin films. Researchers have developed synchrotron X-ray scattering technique with atomic-scale resolution to study ferroelectric thin films and provide insight into the structural gradients at surfaces and interfaces [70–74]. Fig. 4(a) shows the Curie temperature T_C of PbTiO₃ determined through synchrotron X-ray scattering [65]. The satellite peak intensities around the PbTiO₃ 3 0 4 peaks were plotted versus temperature for various thicknesses. The position where the satellite intensity suddenly drops to zero is identified as T_C . X-ray photoelectron diffraction, which applied mostly to investigation of surface and interfacial chemical properties, were also employed to directly probe the intracell atomic displacements associated with ferroelectricity [75]. Recently, Raman has played an increasing important role in determining the ferroelectric phase of thin films. A ferroelectric phase transition is accompanied by a structural change and thus related to specific phonon mode that changes across the Curie temperature. Studying the mode structure in thin films advances our understanding of the ferroelectric phase transition in constrained geometries (see, recent review [76]). By incorporating ultraviolet (UV) illumination, researchers use UV Raman to study symmetry, transition temperature, and phase behavior in much thinner ferroelectric thin films as the penetrating depth of UV is limited and thus the signal from the film is enhanced [66,77]. Fig. 4(b) displays the temperature evolution of Raman spectra for two superlattice samples $([\text{BaTiO}_3]_2/[\text{SrTiO}_3]_{13}) \times 20$ and $([\text{BaTiO}_3]_8/[\text{SrTiO}_3]_4) \times 10$. The shape and position of the BaTiO₃ lines at low temperatures are indicative of BaTiO₃ in tetragonal phase. The red arrows mark the SrTiO₃-like phonons. The intensities of the phonons decrease as the temperature increase and completely disappear at T_C [66]. Other methods that are used to determine the ferroelectric transition temperature include X-ray diffraction (XRD) and second harmonic generation (SHG). XRD can provide temperature dependence of out-of-plane lattice parameter of the strained film, and a kink is typically associated with the transition temperature T_C [12,13,78], as shown in Fig. 4(c). SHG is a nonlinear optical process and only non-centrosymmetric structures are capable of emitting SHG signal. As ferroelectrics must lose the inversion symmetry when they are cooled through T_C , SHG can be used to determine the transition temperature with high accuracy [63,79]. Fig. 4(d) shows the SHG signal from a bulk BaTiO₃ single crystal (circles) and strained BaTiO₃ thin films (squares). The kink in the SHG-temperature plot occurs at the same temperature as does the kink in the out-of-plane lattice parameter versus temperature, both indicating the transition temperature T_C [13].

In recent years, piezoresponse force microscopy (PFM) has emerged as one of the most important techniques to study the electromechanical behavior of various materials at the nanoscale [80]. By symmetry considerations all ferroelectrics must be piezoelectric. PFM can be used to probe tensorial properties between electric field and mechanical strain. It utilizes a basic experimental setup of atomic force microscopy (AFM). A metallic tip under voltage bias is brought in contact with a piezoelectric sample, and the resulting deformation of the sample is monitored through the mechanical displacement of the cantilever tip. The most straightforward and useful application of PFM is to map ferroelectric domains based on variations of the amplitude and phase information when an AC voltage is applied to the conductive tip. Fig. 5 shows an example of using PFM to map the polarization variants and domain structures in BiFeO₃ [81,82]. The crystalline

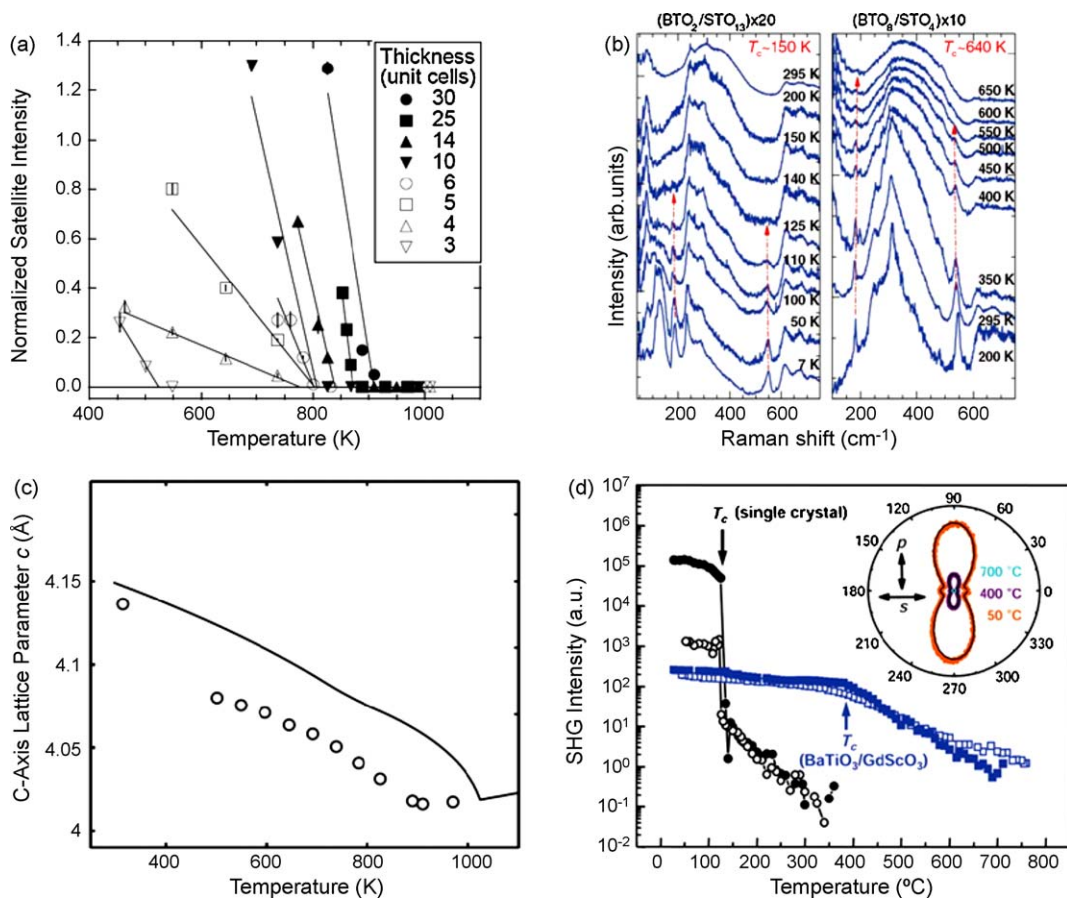


Fig. 4. Curie temperature T_c of ferroelectrics determined using different techniques. (a) T_c determined using synchrotron X-ray scattering, showing intensities of satellite peaks around the PbTiO_3 3 0 4 peak for various thicknesses, normalized to the 3 0 4 peak intensity. The lines are linear fits to determine T_c [65]. (b) Temperature evolution of UV Raman spectra of $\text{BaTiO}_3/\text{SrTiO}_3$ superlattices, showing the SrTiO_3 -like TO_2 mode at 180 cm^{-1} and TO_4 mode at about 530 cm^{-1} which change across T_c [66]. (c) Temperature dependence of the out-of-plane lattice parameter showing a kink at T_c [12]. The line is theoretical prediction. (d) Optical second harmonic generation (SHG) signals from a BaTiO_3 single crystal (circles) and strained BaTiO_3 on GdScO_3 films (squares). The inset shows polar plots of SHG intensity versus fundamental polarization. The kink in the SHG-temperature plot indicates the transition temperature T_c [13].

orientation in the film is typically restricted by the epitaxy. The remaining polarization variables can be determined by knowing the scanning cantilever direction and the contrast in in-plane and out-of-plane images. Compared to electron microscopy, PFM has the advantages of easy operation, nondestructive imaging, and quantitatively mapping ferroelectric domains with high spatial resolution. Therefore PFM is well suited for investigating domain patterns and other polarization-related properties in strained ferroelectric films. Other scanning probe microscopies, such as

scanning nonlinear dielectric microscopy, scanning capacitance microscopy, scanning surface potential microscopies, and scanning near-field optical microscopy are also used to investigate the polarization state of ferroelectrics. (See recent reviews, [83,84])

2.1.2. Results of specific materials

Materials with large coupling between electric field and mechanical strain such as perovskite oxides allow us to probe nontrivial effects induced by epitaxial strain. Note that another

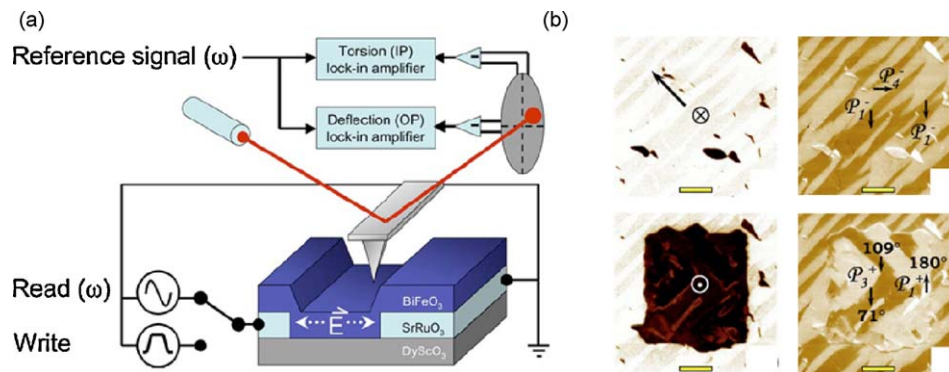


Fig. 5. (a) Schematic view of planar electrode piezoelectric force microscopy (PFM) setup for imaging BiFeO_3 polarization variants. Conductive epitaxial SrRuO_3 electrodes embedded in the film plane will supply an AC field that excites a piezoresponse in the BiFeO_3 [81]. (b) Examples of out-of-plane and in-plane PFM images. Combined with the scanning crystalline direction and PFM images, the three-dimensional domain structures in BiFeO_3 can be determined [82].

type of electromechanical coupling between strain gradient (as opposed to strain only) and polarization, i.e., flexoelectricity [85], is also frequently addressed in thin films and nanoscale materials, especially in the case of inhomogeneously strained ferroelectric thin films. Here we only focus on intrinsic strain effects on uniformly stressed ferroelectric thin films.

2.1.2.1. Strained PbTiO_3 and $\text{Pb}(\text{Zr}_x\text{Ti}_{1-x})\text{O}_3$ thin films. PbTiO_3 is a prototypical perovskite ferroelectric material which undergoes a cubic to tetragonal phase transition with Curie temperature around 470 °C. Both theoretical calculations and experiments suggest that increasing epitaxial compressive or tensile strain will increase the paraelectric–ferroelectric transition temperatures. Fig. 6(a) shows the stability regions of various domain structures in the misfit strain–temperature phase space for (001)-oriented PbTiO_3 films obtained by phase-field simulations [61]. For a given temperature, the equilibrium domain structures can be single c -domains (large compressive strain), $c/a_1/a_2$ three domain state (intermediate strain), or a_1/a_2 two-domain state (large tensile strain). By incorporating an inhomogeneous domain structure in the electrostatic interaction, the boundary between the regions with $c/a_1/a_2$ and c -domains will shift to lower compressive strain side [86], as shown in Fig. 6(b). A “misfit strain–misfit strain” domain stability diagram was also predicted from different simulations such as thermodynamic calculations and phase-field modeling [86–89]. These two methods provide rather different phase diagrams that are not only quantitatively but also

qualitatively different (Fig. 6(c)). Experimentally the thickness dependence of ferroelectricity in PbTiO_3 films has been intensively investigated. Because both thickness and strain have dramatic effects on the ferroelectric properties, an enhancement of T_C was observed in thicker films but a reduction of T_C also showed up in ultra-thin films [12,48,65,90,91].

$\text{Pb}(\text{Zr}_x\text{Ti}_{1-x})\text{O}_3$ (PZT) is a substitutional solid solution which exhibits good piezoelectric properties and plays a significant technological role in actuators and transducers. As shown in Fig. 6(d), the strain–temperature phase diagram of PZT is composition dependent [92]. The substrate-induced strain always increase the Curie temperature and the maximum is around $x = 0.5$ [92]. Monte Carlo simulations were used to investigate the strain–temperature phase diagram of $\text{Pb}(\text{Zr}_{0.5}\text{Ti}_{0.5})\text{O}_3$ ultra-thin films, and a vortex stripe domain was predicted that is otherwise forbidden in bulk crystal [93]. Experimentally the PZT system was extensively investigated thanks to the availability of high-quality epitaxial PZT films and its convenient phase transition temperatures [35,91,94,95].

2.1.2.2. Strained BaTiO_3 films. Upon cooling to low temperatures, BaTiO_3 undergoes a cascade of phase transitions that pass through cubic, tetragonal, orthorhombic, and rhombohedral structures. Each of the transitions involves a change in spontaneous polarization and lattice parameters, and therefore the substrate-induced strain will have a drastic effect on all the transition temperatures. First-principle calculations as well as phase-field

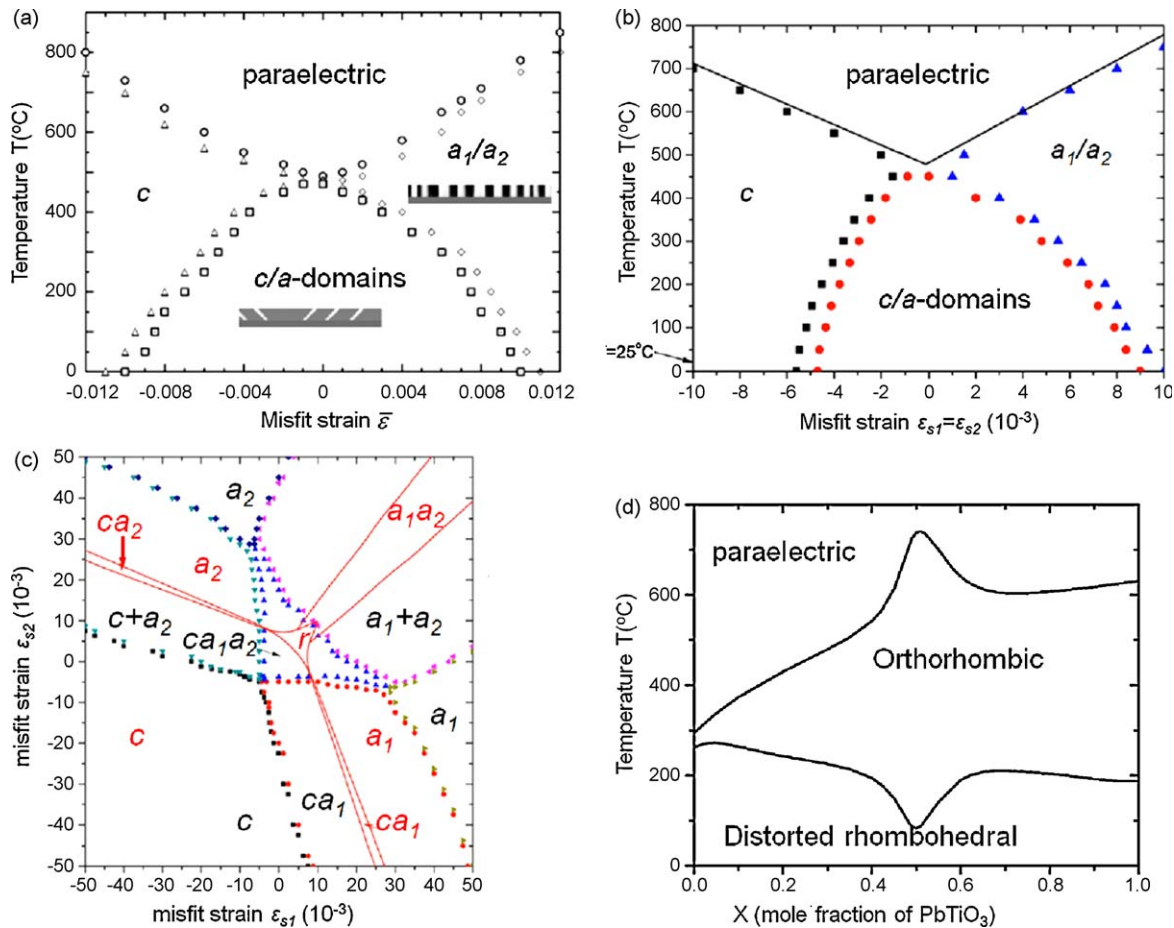


Fig. 6. (a) Domain stability map of PbTiO_3 thin films as a function of temperature and isotropic substrate-induced strain, obtained from phase-field simulations [61]. The two insets are two-dimensional cross section cuts of the corresponding 3D domain structures. (b) Domain stability phase diagram of PbTiO_3 thin films by introducing inhomogeneous domain structures in the electrostatic interactions [86]. (c) “Misfit strain–misfit strain” domain stability diagram for PbTiO_3 thin film at 25 °C. Scattered symbols are from phase-field simulation and the solid lines are from thermodynamic calculation [86]. (d) Phase diagram of PZT film under 0.5% misfit strain obtained from thermodynamic calculations assuming a single-domain state [92].

analysis show that both compressive and tensile strain will elevate the Curie temperature T_C [62,96]. Fig. 7(a) shows the epitaxial strain–temperature phase diagram of BaTiO_3 based on thermodynamic analysis. BaTiO_3 thin films were coherently grown on GdScO_3 and DyScO_3 substrates with a misfit strain of about -1.0% and -1.7% , respectively. The ferroelectric transition temperature shifts to $\sim 400^\circ\text{C}$ on GdScO_3 and $\sim 540^\circ\text{C}$ on DyScO_3 . These values are significantly higher than the T_C of bulk BaTiO_3 at $\sim 130^\circ\text{C}$. It is also observed that the strained thin film has a remnant polarization 250% higher than bulk BaTiO_3 single crystals [13]. Multiple techniques were employed to investigate the ferroelectric properties, including conventional hysteresis measurement for ferroelectricity, and SHG as well as temperature-dependent XRD for determining the Curie temperature. The resulting ferroelectric properties demonstrate a route to Pb-free ferroelectrics for device applications, such as nonvolatile memories and electro-optic devices.

2.1.2.3. Strained SrTiO_3 films. In its pure and unstressed state, SrTiO_3 is not a ferroelectric at any temperature. However, due to the strong coupling between polarization and strain, ferroelectricity is found to be induced by both small compressive and tensile strains. A rich phase diagram has been presented in Ref. [97], showing that the instabilities and their coupling are very sensitive to the misfit strain. Phase-field simulations were used to calculate the ferroelectric and structural domain morphologies at different strain states [63]. The Curie temperature is predicted to increase as the misfit strain increases. Fig. 7(b) shows the predicted shift in T_C for SrTiO_3 under biaxial strain [11]. The shaded region shows the uncertain range in predicted T_C due to the variation in reported property coefficients for SrTiO_3 . This prediction implied that 1% tensile strain would be sufficient to shift the T_C of SrTiO_3 to room temperature. The epitaxial strain-induced room-temperature ferroelectricity in SrTiO_3 thin film was observed by growing the thin film on (1 1 0) DyScO_3 substrates [11]. The strained thin films also display remarkable dielectric properties that were previously only accessible in the bulk at cryogenic temperatures [11]. Recently, anisotropic strain was introduced by growing SrTiO_3 on orthorhombic (1 0 1) DyScO_3 [69]. The anisotropic biaxial strain was found to lead to a new ferroelectric domain reorientation transition that is not observed in isotropically strained films [98].

2.1.2.4. Strained BiFeO_3 films. Ferroelectric BiFeO_3 differs from the previous titanate-based ferroelectrics in that the ferroelectricity in BiFeO_3 derives from the movement of lone pair electrons in Bi ions.

It is reported that BiFeO_3 grown on SrTiO_3 substrate shows an enhanced room-temperature spontaneous polarization that is an order of magnitude higher than that of the bulk [16]. First-principle calculations show that the observed enhancements originate from a high sensitivity of the polarization to small changes in lattice parameters [16]. In contrast to conventional perovskite ferroelectrics, first-principle studies on BiFeO_3 show that the electric polarization of a (1 1 1)-oriented BiFeO_3 film is almost independent of epitaxial strain [99,100]. The magnetization of BiFeO_3 is also independent of strain, although the incorporation of oxygen vacancies can alter its magnetization [100]. Recent thermodynamic calculation shows a strong dependence of spontaneous polarization on substrate-induced strain on (0 0 1) BiFeO_3 thin films [101–105]. The strain dependence of remnant polarization were investigated on the same epitaxial (0 0 1) BiFeO_3 thin film capacitors before and after releasing them from an underlying Si substrate to which they were strained and clamped [106]. The results show that the out-of-plane polarization of (0 0 1)-oriented BiFeO_3 thin films is strongly dependent on strain. Fig. 8(a) shows the misfit strain–temperature phase diagram of (0 0 1) single-domain BiFeO_3 thin films [105]. Similar to other conventional perovskite ferroelectrics, the misfit strain in BiFeO_3 will result in the increase of Curie temperature by either compressive or tensile strain. The ferroelectric domain structures of epitaxial BiFeO_3 thin films were modeled using the phase-field approach, as shown in Fig. 8(b). The domain structures strongly depend on the substrate constraints [107]. The formation of a morphotropic phase boundary via epitaxial strain in BiFeO_3 films was demonstrated recently. As piezoelectric materials are typically characterized by the intimate coexistence of two phases across a morphotropic phase boundary, this discovery makes this Pb-free system highly interesting for probe-based data storage and actuator applications [105].

The control of ferroelectric polarization variants in BiFeO_3 also attracted a lot of attention. The domain patterns were imaged using PFM. Scans taken with the tip field pointing along the principal crystallographic directions enabled researchers to reconstruct the polarization direction from the eight different variants [81,82,108]. By carefully choosing the substrate, one can control the domain pattern at the nanometer scale [109,110]. The stability of domains and domain walls was also investigated and it was observed that strain can result in a drastically different thermodynamic stability of two parallel domain walls with the same orientation [111].

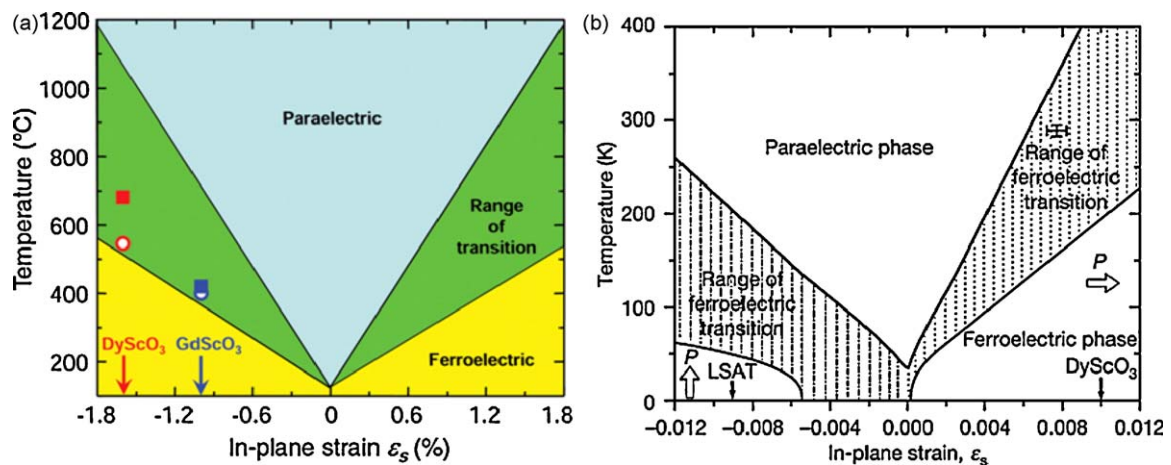


Fig. 7. The epitaxial strain–temperature phase diagram of BaTiO_3 (a) and SrTiO_3 (b) thin films from phase-field analysis [11,13]. The green region in (a) or shaded region in (b) represent the range in the predicted T_C due to the variation of reported property coefficients. (For interpretation of the references to color in this figure legend, the reader is referred to the web version of the article.)

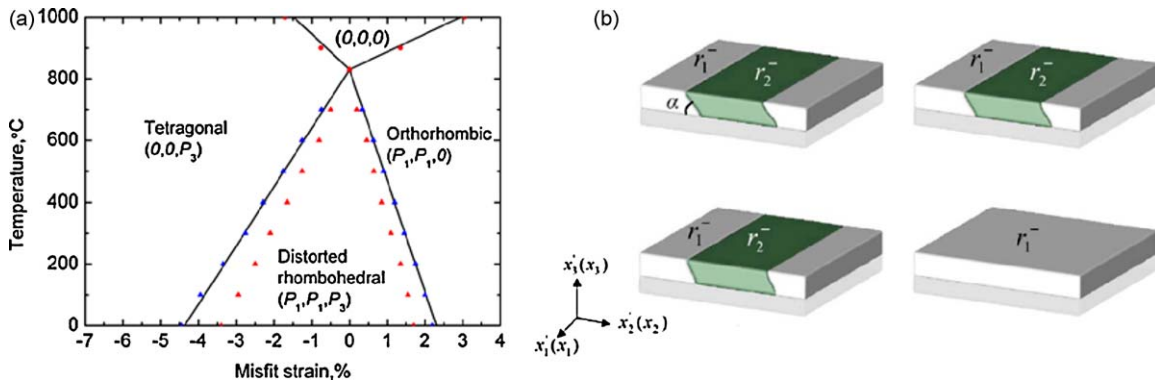


Fig. 8. (a) Phase stability diagram of (0 0 1) BiFeO₃ thin film as a function of temperature and misfit in-plane strain [105]. (b) Domain structures of (0 0 1) BiFeO₃ thin films from phase-field simulations, which corresponds to different substrate constraints [107]. The states are: (top left) $\epsilon'_{11} = \epsilon'_{11} = -0.01$, $\epsilon'_{12} = 0$; (top right) $\epsilon'_{11} = \epsilon'_{11} = 0$, $\epsilon'_{12} = 0$; (bottom left) $\epsilon'_{11} = \epsilon'_{11} = -0.01$, $\epsilon'_{12} = 0$; (bottom right) $\epsilon'_{11} = \epsilon'_{11} = -0$, $\epsilon'_{12} = 0.005$.

2.2. Magnetoresistive manganese perovskites

The observation of colossal magnetoresistance (CMR) effect in doped manganites has attracted considerable attention motivated by desire to understand and improve the electronic and magnetic properties of these materials [112]. This family of compounds have chemical formula $\text{Re}_{1-x}\text{A}_x\text{MnO}_3$, with Re a rare earth such as La or Pr and A a divalent alkali such as Sr, Ca, or Ba. By adjusting the doping level x , the manganites show a rather complicated phase diagram that can be characterized by magnetic, electric, and charge-ordering properties. Upon temperature increase, properly doped manganites exhibit a low-temperature ferromagnetic metallic to high-temperature paramagnetic insulating phase transition and the colossal magnetoresistive effect occurs near the transition. These behaviors can be understood to first-order approximation within the framework of double exchange theory. Recently, it is shown that the double exchange physics alone does not fully explain the CMR effect of manganites, and the strong electron–phonon interaction arising from the Jahn–Teller splitting of the outer Mn d level electrons should be addressed [113–115]. As a result, the application of strain is predicted to have substantial effects on the transition temperature and magnetic properties by modulating the Jahn–Teller splitting.

In addition to the double exchange theory and Jahn–Teller splitting effect, the drastic change in resistivity upon the application of magnetic field has also been interpreted in terms of an electronic phase separation model [116]. In this model, the transition is predicted as a percolative effect. Spatial electronic phase inhomogeneity at the nano- to microscale has been widely observed in strongly correlated electron materials and the origin is still under debate [3]. In manganites, existing theories explain the origin of phase inhomogeneity by either an intrinsic mechanism arising from inherent properties of such strongly correlated electron systems [117,118], or extrinsic mechanisms based on effects of chemical disorder or local strain distribution [119]. If the phase separation is extrinsically induced by elastic strain, lattice strain may provide an effective way to engineering the phase transition and domain pattern.

2.2.1. Phase separation and domain pattern

Spatial phase inhomogeneity or domain structures have been observed in CMR manganites, where multiple phases such as ferromagnetic metallic (FMM) and antiferromagnetic insulating (AFI) phases coexist at nano- to microscale at temperatures where a pure phase is expected [120–124]. This phase separation is believed to be fundamentally related to the CMR effects in manganites [116]. In the presence of quenched disorder, the two

states are nearly degenerate and therefore they can coexist. In this regime, small perturbations such as magnetic field can drastically change the properties of the materials and globally driver the system to the FMM phase [3].

Despite decades of investigation, the question of whether the phase inhomogeneity is intrinsic or caused by external stimuli (extrinsic) still remains open. The nanoscale inhomogeneity is typically explained by electronic phase separation, where charge density is an order parameter in the simulations. The long-range Coulomb interaction is not included in the model. When quenched disorder is included, by incorporating long-range effects, such as Coulomb forces or cooperative oxygen octahedral distortion [117,125], the system will develop inhomogeneous phases. Calculations incorporating elastic energy only [119], or within a phenomenological Ginzburg–Landau theory [126], could also lead to inhomogeneous phase patterns. The theory of strain-induced metal–insulator phase coexistence in manganites is of special interest [119]. In this model, the phase with short and long-wavelength lattice distortions is insulating and that without lattice distortion is metallic. The structural aspect will be the primary reason that causes the multiphase coexistence. As shown in Fig. 9, the relaxed system tends to contain distorted insulating regions due to the extended long-range correlations. In this model, the domain formation is self-sustained. External stimuli such as strain can be used to sensitively manipulate patterns of metallic and insulating regions and thus makes possible the control of nano-engineered functional domains in manganites. The idea of strain-induced metal–insulator phase separation was tested recently [127]. Researchers were able to induce anisotropic electronic domains along a preferential orientation of $\text{La}_{5/8-x}\text{Pr}_x\text{Ca}_{3/8}\text{MnO}_3$ ($x=0.3$) (LPCMO) thin film by epitaxially locking it to an orthorhombic NdGaO_3 (NGO) substrate. As shown in Fig. 10, interesting anisotropic properties were observed in this system, which indicate that the percolative conduction channel is anisotropic. These findings suggest that the origin of phase coexistence can be strongly influenced by elastic energy rather than local chemical inhomogeneities [127]. The evolution of phase domains in double-layer manganite $\text{Sr}_3(\text{Ru}_{1-x}\text{Mn}_x)_2\text{O}_7$ under mechanical stress was also imaged with electron microscopy and the results point toward the important role of strain in phase separation [128]. Although the exact origin of the phase separation is still under debate, its importance to understanding the manganite physics is now widely accepted.

2.2.2. Effects on transport properties

If elastic strain is the reason that induce the phase separation, it can definitely affect the transport properties of CMR thin films

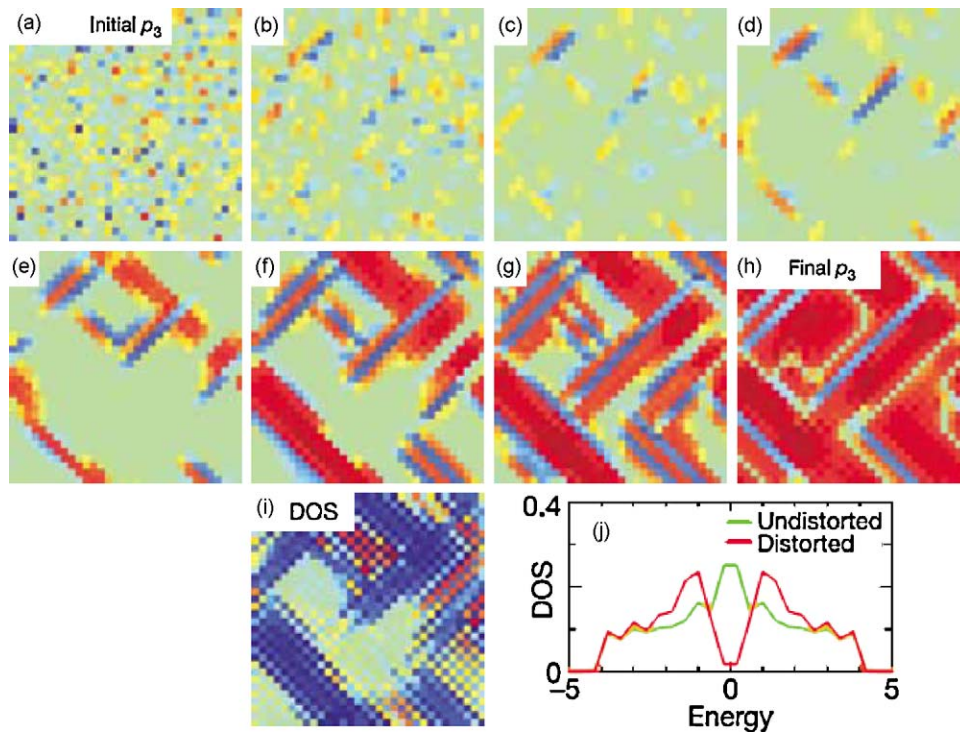


Fig. 9. Simulations for strain-induced metal-insulator phase coexistence in perovskite manganites [119]. (a) The $p_3 = s_x^2 - s_y^2$ field initial configuration, where s_x and s_y represent the short wavelength modes. (b)–(g) Time-sequence of p_3 during energy relaxation. (h) Final stable stage. (i) and (j) Electronic properties obtained by numerically solving the Su–Shrieffer–Heeger Hamiltonian on the elastic templates.

through redistribution of the inhomogeneous phases [127]. There are several other structural effects on electronic properties in manganites. One structural influence is that lattice strain can distort the Mn–O–Mn bond angles away from 180° or enlarge the length of Mn–O bonds length so that the electronic band width will be reduced. As a consequence, the ferromagnetic double exchange interaction will decrease and therefore the electric and magnetic properties of the manganites will be affected [129]. The other important structural effect originates from the Jahn–Teller electron–phonon coupling [113]. In the cubic perovskite-type lattice, the Mn $3d e_g$ level is twofold degenerate in octahedral MnO_6 coordination but the degeneracy is lifted by a uniaxial distortion of the octahedron. The epitaxial strain in films will have similar effect since it favors certain e_g electron orbitals. Therefore strain that reduces the Jahn–Teller splitting will increase the electron hopping amplitude, while strain that increases the Jahn–Teller splitting will make the electrons to become more localized [113]. If the film is originally in nearly cubic lattice, both tensile and compressive strains tend to reduce the Curie temperature (T_C) and saturated

magnetization (M_{sat}). On the other hand, if the film originally adopts non-cubic lattice, it is possible that the biaxial strain will enhance the transition temperature. Numerous investigations have been carried out in investigating the effect of substrate misfit strain on the electric and magnetic properties of manganite thin films. $La_{0.7}Sr_{0.3}MnO_3$ has a nearly cubic structure, and the ferromagnetic Curie temperature has been reported to decrease regardless of the sign of imposed strain [25,130–132], as shown in Fig. 11(a). The strain dependence of T_C in manganites was also quantified using phenomenological models and it was found that 1% biaxial strain would cause a 10% shift in T_C [114].

Experimentally the relationship between T_C (and/or other electric and magnetic properties) and lattice strain can be very complicated, as the properties of manganites are sensitive not only to strain, but also to other extrinsic variables including oxygen vacancies, crystalline quality, thickness, compositional variation, grain boundary, dead layer, etc. It is therefore very difficult to rule out the effects of these extrinsic variables when studying the strain effect using a series of thin films with different thickness. Due to

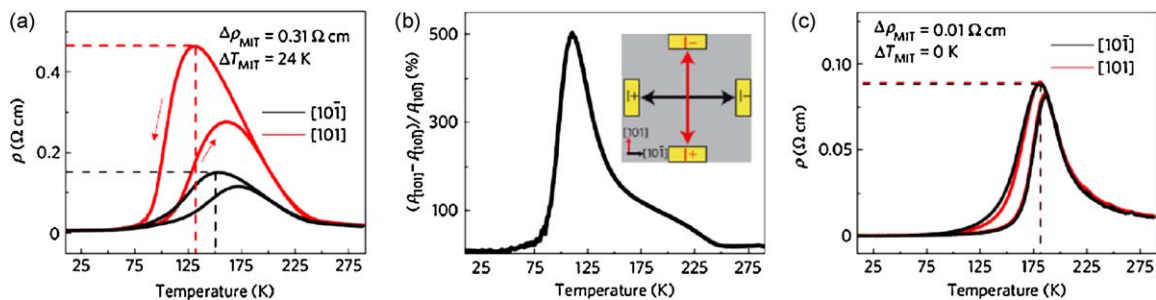


Fig. 10. (a) LPCMO film on an NGO substrate has anisotropic in-plane strain and shows significant difference in both the MIT temperature and the resistivity at the MIT depending on which axis the transport is across. (b) Relative percentage difference between cooling curves along perpendicular in-plane directions (c) LPCMO film with isotropic in-plane strain grown on SrLaGaO₄ substrate showing negligible differences in transport properties along the two in-plane axes [127].

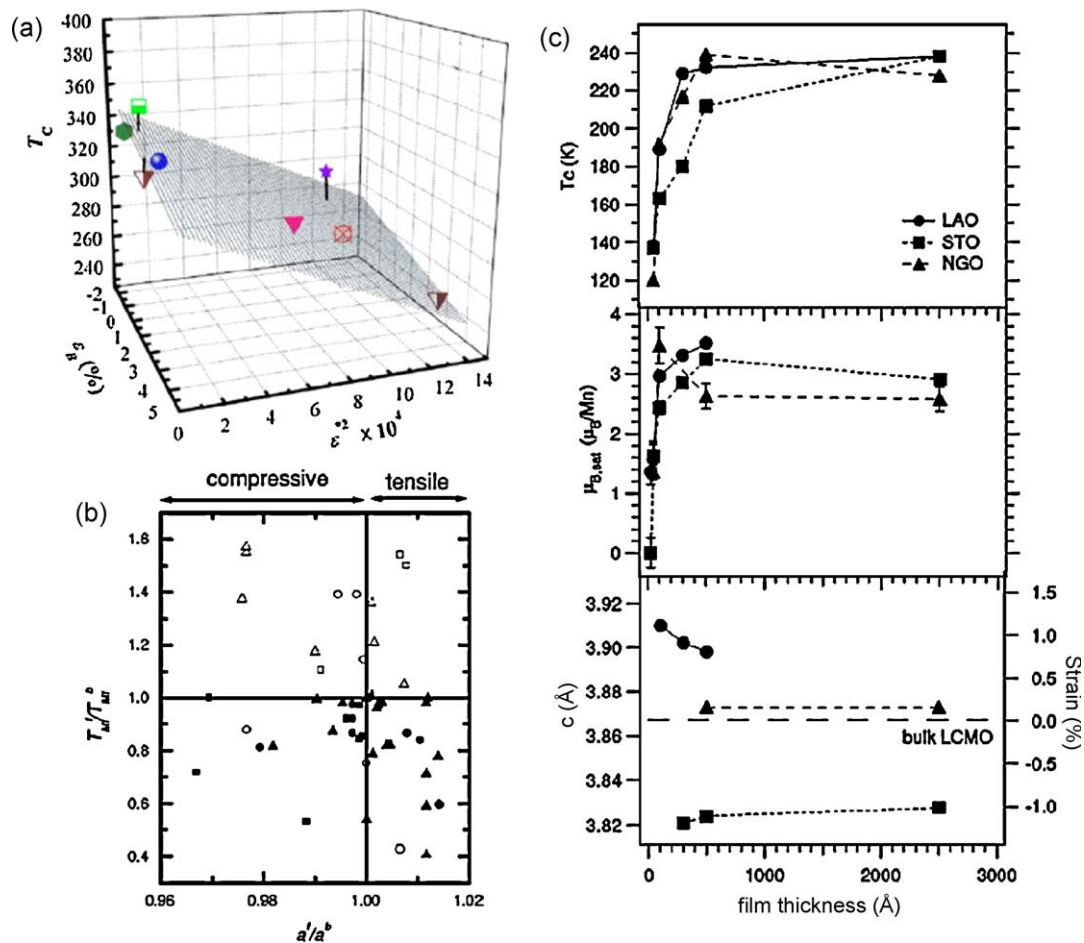


Fig. 11. Strain effect on the magnetic properties of manganite thin films. (a) The Curie temperature T_C versus then ϵ_B and ϵ^x strains. $\text{La}_{0.7}\text{Sr}_{0.3}\text{MnO}_3$ films were grown on different substrates with misfit strain ranging from -2.3% to $+3.2\%$ [25]. (b) Effect of strain on the transition temperature in Ca-doped (triangle), Ba-doped (square) and Sr-doped (circle) LaMnO_3 films from different literature [133]. Open symbols and closed symbols refer to underdoped ($x < 0.3$) and above-optimal-doped regimes ($x \geq 0.3$), respectively. (c) T_C , M_{sat} , and out-of-plane lattice constant versus the thickness of the $\text{La}_{2/3}\text{Ca}_{1/3}\text{MnO}_3$ thin films [134].

these reasons, a lot of controversial results have been reported and discussed in $\text{La}_{1-x}\text{A}_x\text{MnO}_3$ ($A = \text{Ca}, \text{Sr}, \text{Ba}$) films. For example, Lu et al. reported that the T_C of $\text{La}_{2/3}\text{Ba}_{1/3}\text{MnO}_3$ decreased with increasing tensile biaxial strain [26,135]. Several other groups reported that tensile strain would increase T_C and reduce the resistivity in the case of $\text{La}_{1-x}\text{Ba}_x\text{MnO}_3$ ($x < 0.2$) [14,136–139]. In contrast, Murugavel et al. reported that, irrespective of whether the substrate misfit strain is compressive or tensile, doping level strongly affects the transport properties of $\text{La}_{1-x}\text{Ba}_x\text{MnO}_3$ [133,140,141]. Fig. 11(b) shows the relative ratio of T_{MI} values between films and bulk as a function of substrate-induced strain, taken from various literature [133]. It was argued that the substrate-induced strain does not have a systematic effect on the transition temperature. On the other hand, the doping level strongly influence T_{MI} , as almost all the underdoped ($x < 0.3$) manganites (open symbols) have enhanced transition temperatures and the above-optimal-doped ($x \geq 0.3$) (closed symbols) show decreased T_{MI} . Orgiani et al. found similar effects that oxygen nonstoichiometry greatly influence the transport properties and T_C of $\text{La}_{0.7}\text{Ba}_{0.3}\text{MnO}_3$ thin films [142]. Actually, whether or not the magnetic properties of manganites are modified by strain was also in debate. Despite the very controversial results of strain effects on T_C and M_{sat} of $\text{La}_{2/3}\text{Ca}_{1/3}\text{MnO}_3$ [143–146], it was reported that these properties can be suppressed by reduction of the film thickness [134]. Fig. 11(c) displays the magnetic and structural properties as a function of thickness. By depositing $\text{La}_{2/3}\text{Ca}_{1/3}\text{MnO}_3$ films on different substrates, a wide range of in-plane biaxial strain from

tensile ($+0.98\%$ SrTiO_3), essentially zero (-0.10% NdGaO_3), to compressive stress (-1.99% LaAlO_3) were established. Despite the different structural response from different substrates, all the films exhibit a thickness dependent T_C and M_{sat} . Even for the non-strained film on NdGaO_3 substrate, a suppression of T_C and M_{sat} was observed [134]. These findings indicate that the decrease in T_C and M_{sat} might be due to the two-dimensional nature of the films instead of the strain.

In order to investigate the intrinsic lattice strain effect, researchers recently developed a dynamic way to produce biaxial strain in thin film by *in situ* inducing lattice strain in substrates on the same thin film sample [22,147–154]. $\text{La}_{1-x}\text{A}_x\text{MnO}_3$ ($A = \text{Ca}, \text{Sr}, \text{Ba}$) films are epitaxially grown on piezoelectric $(1-x)\text{Pb}(\text{Mg}_{1/3}\text{Nb}_{2/3})\text{O}_3-x\text{PbTiO}_3$ (or PMN–PT) single crystals. The lattice constant of PMN–PT is larger than that of $\text{La}_{1-x}\text{A}_x\text{MnO}_3$ films, making the thin film be locked in a tensile strain state. Through the ferroelectric poling or the converse piezoelectric effect, the strain of the thin film can be varied *in situ*. An increase of the electric field applied to the PMN–PT substrate will increase the out-of-plane strain of the substrate, and consequently, induce the in-plane compressive strain. The induced in-plane compressive strain in the PMN–PT substrate can be transferred to the $\text{La}_{1-x}\text{A}_x\text{MnO}_3$ film and thus cause a decrease in the biaxial tensile strain of the films. Consistent decrease in resistivity and increase in T_C were observed in $\text{La}_{1-x}\text{A}_x\text{MnO}_3$ thin films [22,147–154] as the tensile strain decreases. By ruling out the extrinsic effects such as growth conditions, crystalline quality, etc., these *in situ* experiments

demonstrate that strain indeed has strong effects on the electric properties of $\text{La}_{1-x}\text{A}_x\text{MnO}_3$ films through the Jahn–Teller electron–lattice coupling.

3. Strain effects in TMO micro/nanowires

3.1. Electromechanics in TMO micro/nanowires

The coupling between electric field and mechanical strain in piezoelectric materials has made them the most promising candidates for converting mechanical energy into electricity. Energy harvesting using piezoelectrics has received considerable attention due to their potential applications as sustainable and maintenance-free power sources to replace traditional batteries. Piezoelectricity only occurs in non-centrosymmetric crystals by crystallographic considerations. Recently both theory and experiments suggest that, the coupling between the polarization and strain gradient, i.e., flexoelectricity, can become very important in electromechanical effects. Theoretical calculations also predicted that, when the size of piezoelectrics is limited to a narrow range, the efficiency of a nanoscale piezoelectric power generator may increase significantly (500% in the case of BaTiO_3) under inhomogeneous strain due to the flexoelectric effect [155,156]. Flexoelectricity was also employed to fabricate piezoelectric composites without using piezoelectric materials [157–160]. Here the composites are fabricated using mixed non-piezoelectric components with a textured symmetry. Upon the application of a uniform stress, a non-uniform strain field or strain gradients will be created and locally break the inversion symmetry [157–160]. As the induced strain gradients increase as the composite dimensions decrease, the piezoelectric performance of such meta-materials would be enhanced with size reduction [159]. Strain gradient-induced polarization has also been observed in SrTiO_3 single crystals [161]. Exploitation of flexoelectricity and the associated nanoscale size effects can lend more insights for future design of electromechanical systems.

The ability for harvesting environmental mechanical energy at small scales using nanomaterials is also a key component to integrated nanodevices. As the low power capacity of nanosized battery will severely limit the lifetime of the entire system, a nanogenerator that could continuously scavenge the environmental energy is essential to building self-powered nanosystems. Researchers have demonstrated different approaches to convert mechanical energy into electricity using piezoelectric nanowires. For examples, Wang et al. observed a periodic voltage generation by applying periodic tensile mechanical load on individual BaTiO_3 nanowires [162]. Similarly, Dr. Z.L. Wang's group employed a wide variety of innovative nanotechnology-enabled methods to investigate mechanical energy harvesting by ZnO nanowires [43,163–168]. Compared to other energy harvesting technologies such as photovoltaics and thermoelectrics, the nanowire-based nanogenerators have the advantages of good performance under harsh conditions, strong resistance to fatigue, high sensitivity to mechanical vibration, and large surface area for surface functionalizations.

Applicable piezoelectric materials are typically insulating, as free charges will immediately screen the piezoelectric potential once it is generated. ZnO nanowires with moderate conductivity are able to preserve the potential for a sufficiently long time after the mechanical deformation, which is likely caused by strong trapping effects of the free carriers by vacancy, impurity, and/or surface states in ZnO [169]. Although the piezoelectric constant in ZnO is relative low compared to that of BaTiO_3 or $\text{Pb}(\text{Zr}_x\text{Ti}_{1-x})\text{O}_3$, ZnO nanowires and nanobelts have received more attention in recent years with promised applications in nanogenerators and nanopiezotronics. The main advantages are that ZnO nanowires

can be relatively easily grown on all kinds of materials (crystalline or amorphous, hard or soft) in regular arrays, and ZnO itself is biocompatible and nontoxic to the environment. Therefore, they can be integrated into other technologically important materials for a wide range of applications. Studies on developments of ZnO nanotechnology were extensively covered in two recent reviews [43,164].

3.2. Phase transitions and domain physics under strain

As discussed in previous sections, many bulk TMOs exhibit phase transitions where a spatial phase inhomogeneity or multiple domains exists near the transition temperature, which obscures experimental studies of their intrinsic properties. TMO nanomaterials can be made in size comparable to the characteristic domain width, making them suitable to explore domain dynamics and fundamental phase transition physics. In addition, as nanomaterials are typically single crystals and dislocation-free, they can sustain an extremely large elastic strain without plastic deformation or fracture. Stressing the nanomaterials to exceedingly high values enables exploration of the fundamental physics at unprecedented levels. Investigation of the physical properties with response to strain in TMO nanowires at small length scales has recently attracted intense research attention. Vanadium dioxide (VO_2) is a representative TMO that exhibits a coupled electronic and structural transition, thus offering an interesting platform to study its phase transition at the single-domain level.

3.2.1. Phase inhomogeneity and domain organization

VO_2 undergoes a first-order metal to insulator transition (MIT) at 341 K with a change in conductivity by several orders of magnitude [170,171]. The MIT is accompanied by a structural phase transition from the high-temperature tetragonal phase to the low-temperature monoclinic phase [170,172]. Upon cooling through the MIT, the vanadium ions will dimerize and the pairs tilt with respect to the tetragonal *c*-axis, causing the specimen to expand by 1% along the *c*-axis [170,172]. As expected from the abrupt change in lattice constant upon the phase transition, a uniaxial compressive (tensile) stress along the tetragonal *c*-axis direction would drive the system toward the metallic (insulating) phase. This electronic-structural coupled phase transition is manifested with complex yet interesting properties that have been under investigation for decades.

Depending on whether a stress is imposed on the sample or not, VO_2 shows rather distinct optical and electronic properties. As shown in Fig. 12(a), devices made from unstrained sample will display a sharp drop of resistance at 341 K (single-domain device), accompanied by an abrupt change in optical reflection, with dark reflection corresponding to metallic phase and bright reflection to insulating phase. On the other hand, the electrical resistance of the clamped VO_2 beams decreases gradually over a wide phase transition temperature range (multiple-domain device). Optical imaging of the clamped beams in Fig. 12(b) revealed that the broadening of transition is due to the nucleation and growing/shrinking of metallic/insulating domains as a function of temperature [173]. The electrical and optical properties of VO_2 thin films share similar behavior as that of the clamped VO_2 beams. As shown in Fig. 12(c and d), the resistance–temperature curve shows a gradual change between 341 and 343 K that corresponds to the multiple phases coexistence [174]. In this work, the phase of VO_2 during the gradual resistance change was referred to as a “strong correlated metal”. Combined with near-field and far-field experiments, and effective medium theory analysis, it was concluded that the metallic puddles show divergent quasi-particle mass with a pseudogap existing in the “strong correlated metal” region [174]. In contrast, recent infrared studies on strain-free, single-domain

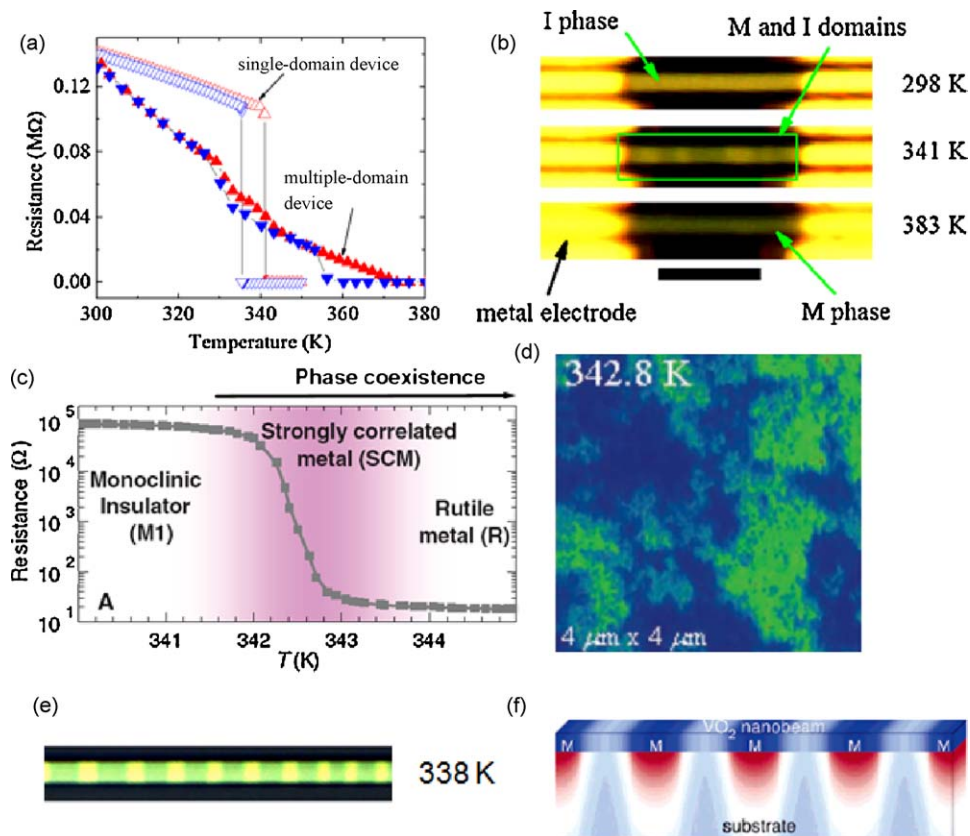


Fig. 12. (a) Four-probe resistance of single-crystal VO_2 beams as a function of temperature. The free-standing VO_2 beam shows single-domain behavior, whereas the clamped beam shows multiple domains during the transition. (b) Optical images of the multiple-domain devices, showing the coexistence of metallic (dark) and insulating (bright) domains at intermediate temperatures [173]. The scale bar is $5 \mu\text{m}$. (c) Resistance–temperature curve of a VO_2 thin film, showing the broadening of the phase transition. (d) Images obtained by scattering scanning near-field infrared microscope showing the coexistence of metallic (green) and insulating (dark blue) phases of a VO_2 thin film [174]. (e) Optical image of clamped VO_2 at 338 K showing periodic metallic and insulating domains. The width of the VO_2 beam is around $1.5 \mu\text{m}$. (f) Schematic diagram showing the periodic domain pattern of a VO_2 beam coherently strained on a SiO_2 substrate [175]. (For interpretation of the references to color in this figure legend, the reader is referred to the web version of the article.)

VO_2 samples revealed that the phase transition is very abrupt. The metallic puddles with divergent effective mass and pseudogap that were proposed in thin films were not observed in such single-domain VO_2 crystals [176]. Therefore, work on samples with size smaller than the characteristic domain size helps to reveal intrinsic properties of complex oxides in the homogeneous limit that are hidden from experiments on multiple-domain samples [176]. In strained VO_2 beams, the multiple-domain coexistence can be understood through analysis of energy minimization [175]. A fully coherently strained VO_2 beam bottom clamped on the substrate exhibits periodic domains (Fig. 12(e)). Such a domain pattern forms spontaneously as a result of competition between strain energy in the elastically mismatched VO_2 /substrate system and domain-wall energy in the VO_2 (Fig. 12(f)). The period of the pattern is determined by the balance between the strain-energy minimization that favors small, alternating metallic-insulating domains and domain-wall energy minimization that opposes them [175].

3.2.2. Investigation of phase transition at the single-domain level

By investigating the electrical and optical properties of VO_2 at the single-domain level, it is possible to discover new properties of its phase transition in unprecedented detail. For example, it has been a topic of debate for decades that whether the MIT is fundamentally driven by electron–electron correlation, therefore is a Mott transition, or by electron–lattice interaction, therefore a Peierls transition [179–181]. In the Mott transition picture, the insulating phase is a Mott insulator where the bandgap opens because of Coulomb blockade between strongly localized d

electrons at the vanadium sites. In the Peierls transition picture, the bandgap exists because of lattice potential modulation by the vanadium dimerization. There are many experimental evidences that support both mechanisms [179–181]. The controversy is largely due to the poorly understood near-threshold behavior in thin films or bulk crystals, where phase separation and domain formation prevent direct measurements of intrinsic electronic and optical properties. To circumvent this issue, the electrical properties of VO_2 beams were investigated at the single-domain level. As shown in Fig. 13, when the beam is clamped onto a substrate at its two ends, VO_2 was forced to move along the metal/insulator phase boundary in the stress–temperature phase space, and a constant resistivity was observed for the insulating phase [177,178]. More detailed experiments to test such a constant threshold resistivity over a wider range of space including both tensile and compressive states were also performed [182]. It was theoretically demonstrated that, although temperature and stress are two independent experimental parameters, when both are being turned to the threshold of MIT, the effect of increasing thermal excitation is exactly counter-acted by the effect of bandgap widening, such that a constant threshold resistivity is maintained [182]. The constant threshold resistivity means that the transition to the metallic phase occurs only when the electron density reaches a critical strength. Such a constant carries density indicates that the MIT is triggered fundamentally by electrostatics in the system, because the non-degenerate carrier density is not sufficiently high to directly distort the energy bands or stabilize a different lattice structure.

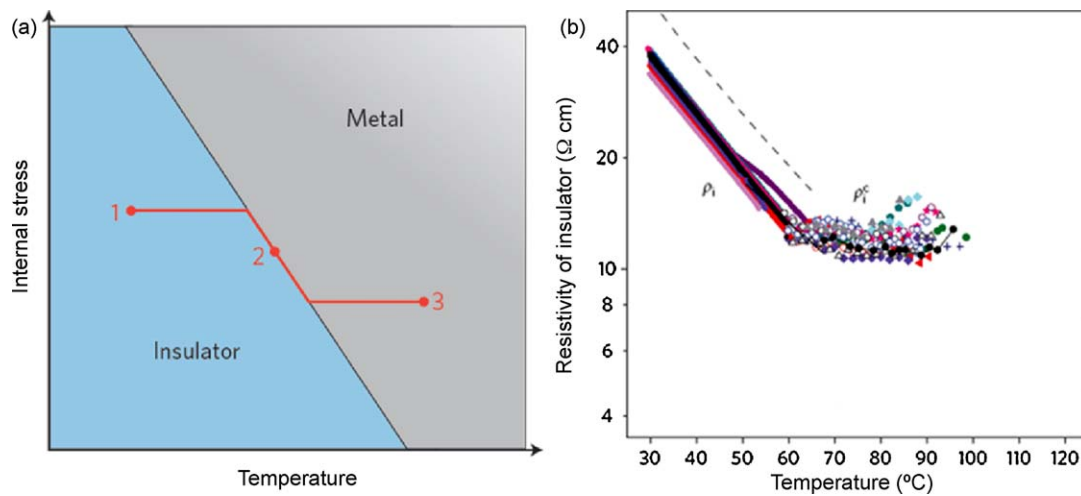


Fig. 13. (a) Schematic view of the path for a fixed length VO₂ beam moving in the uniaxial stress–temperature phase diagram [177]. (b) Resistivity of the insulating phase of VO₂ as a function of temperature. A constant resistivity (at 60–100 °C) is observed when the system moves along the phase boundary [178].

3.2.3. Superelasticity in phase transition

Superelasticity (or pseudoelasticity) has been widely observed in shape memory alloys, where an applied stress can cause a reversible phase transformation between the austenitic and martensitic phases of a crystal [183]. The superelasticity originates from the reversible creation and motion of domain boundaries during the phase transformation rather than from bond stretching or the introduction of defects in the crystal lattice. TMOs are typically brittle and can only be stretched or compressed for an extremely small percentage. In TMOs with phase transitions, control of the domain-wall motion may provide an effective way to realize superelasticity. This effect has been recently demonstrated in the first-order MIT of VO₂ [184]. An AFM tip was used to bend a VO₂ nano-cantilever and the force–displacement (f – w) curves was recorded, as shown in Fig. 14(a) and (c). At small deflections, the f – w curve is linear as expected [184]. The slope of this linear part can be used to determine the Young's modulus of VO₂. At large deflections (but still within the reversible, elastic regime), VO₂ beam shows superelasticity, as evidenced by the appearance of kinks and nonlinearity. These kinks are reproducible upon repeated bending of the VO₂ nanobeams and occur at lower displacements at temperatures that are closer to the natural transition temperature (T_0^c). At the same degree of deflection, no such kinks were observed when bending nanobeams with similar size but made of materials without phase transition, such as ZnTe nanowires. Fig. 14(b) shows optical images of side-bending a wider VO₂ beam, which suggests that the nonlinearity and kinks in the f – w curve is related to the creation and motion of new domains. Phase-field modeling was also used to simulate the f – w curve and obtained qualitatively similar results, as shown in Fig. 14(d).

The superelastic behavior observed during the MIT in VO₂ provides a new route to investigate the solid–solid phase transitions in general. The dynamics of force–displacement curve during the transition can be easily understood by comparing it with the condensation–evaporation process between a liquid and its vapor. When the vapor is compressed isothermally below the critical temperature, the pressure first increases following the ideal gas law, then reaches a plateau where liquid droplets nucleate out of the vapor forming a liquid–vapor coexisting system [185]. In this coexisting state the compressibility of the system diverges, because the decrease in total volume is accounted for by the conversion of more vapor into much denser liquid, rather than to increase pressure as in the pure ideal gas. The pressure–volume curve in this system is equivalent to the f – w curve in VO₂

nanobeam. At temperatures lower than the natural transition temperature, the bottom edge at the root of the nanobeam will be compressively stressed with increasing bending. At a critical compressive stress, new metallic domains start to nucleate out of the original insulating phase, and the bottom portion of the nanobeam root enters a metal–insulator phase coexisting state. As the nanobeam is further bent beyond the critical stress, the metallic domains start to grow in response to the increasing uniaxial compression and a vanishing Young's modulus is expected from the metal–insulator coexisting part (bottom portion) of the nanobeam. The top portion of the nanobeam is under tension and therefore remains in the original insulating phase. The overall Young's modulus measured is the effective Young's modulus of the “composite” beam and therefore a lower but non-zero slope of the f – w curves is observed in this region. At temperatures higher than the natural transition temperature, similar scenario exists except that now new insulating domains nucleate out of the metallic phase in the top portion of the nanobeam as a result of the maximum tensile stress there [184].

3.2.4. Domain dynamics and manipulation

The dynamics of domains in response to external stimuli are also attractive as they provide an effective route to control and manipulate the domains at small scales. A current-driven phase oscillation and domain-wall propagation have been observed in tungsten-doped VO₂ nanobeams [186]. The domain oscillation occurs through the axial drift of a single metallic–insulating domain-wall driven by a combined effect of Joule heating and Peltier cooling. Through actively bending single VO₂ beams, it has been shown that strain can produce ordered arrays of metallic and insulating phases along the length [173]. Fig. 15(a) shows the development of an array of triangular domains along a bent VO₂ beam imaged at different temperatures [173]. Metallic domains nucleate out of the insulating phase at elevated temperatures, and the system reaches a 50–50% coexistence of metallic and insulating domains at the natural phase transition temperature. The dynamics of the domain evolution can be successfully captured through phase-field modeling, as shown in Fig. 15(b). In particular, strain was also used to lower the temperature of the transition from its bulk value of 341 K to room temperature, which paves the way for future potential applications. Enabled by the sensitivity of the electronic phases to local strains, external stress was used to manipulate and engineer these functional domains. As displayed in Fig. 15(d) [173], an array of metallic–insulating triangular domains

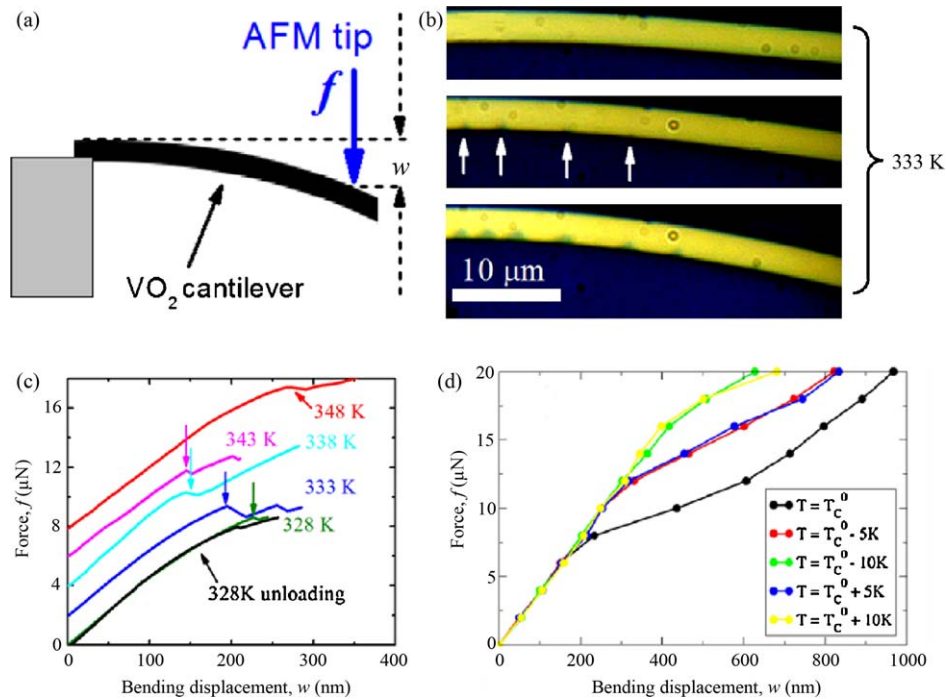


Fig. 14. Superelastic metal–insulator phase transition in VO_2 beams. (a) Schematic view of bending a VO_2 nano-cantilever using an AFM tip. (b) Optical images of side-bending a wide VO_2 beam, showing the nucleation of new domains with increasing stress. (c) Force–displacement curves of a VO_2 cantilever measured at various temperatures. The curves are vertically offset for clarity. Arrows show the position of the first kink on each curve. (d) Simulated force–displacement curves for a beam demonstrating the slope change that occurs at the onset of new domain formation [184].

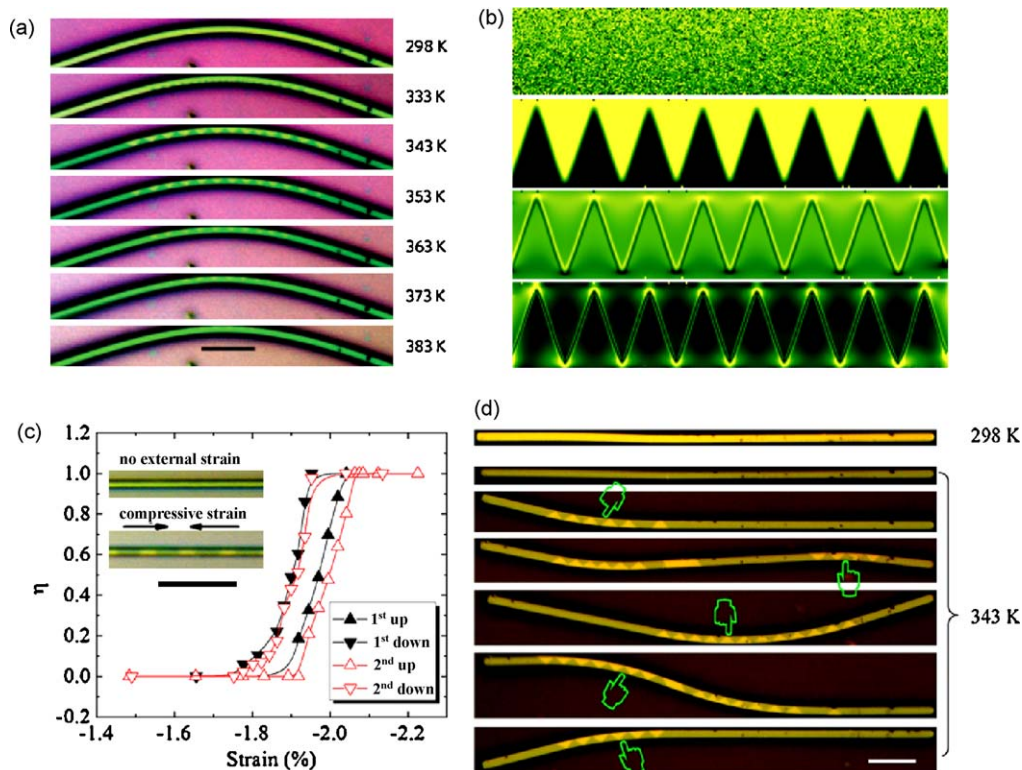


Fig. 15. Domain dynamics and manipulation with strain in VO_2 [173]. (a) Optical images of an array of triangular metallic domains nucleated and co-stabilized by tensile and compressive strain along a bent microbeam. (b) Phase-field modeling of domain formation in a bent VO_2 beam. From top to bottom: First, initial state of random phase distribution; Second, equilibrium phase distribution at the natural MIT transition T_c^0 ; Third, equilibrium strain (ϵ_{xx}) distribution at T_c^0 : yellow and dark green denote the maximum tensile and maximum compressive strain, respectively; Forth, Equilibrium strain-energy density distribution: yellow denotes the highest strain-energy density; dark green denotes the lowest. (c) Uniaxial compression reversibly induces a metal–insulator transition at room temperature. Here η is the fraction of metal phase along the beam. (d) Strain engineering domains in a flexible VO_2 microbeam. Scale bars in (a), (c), and (d), 10 μm . (For interpretation of the references to color in this figure legend, the reader is referred to the web version of the article.)

are created and eliminated by simply modulating the local strain state of a bent VO₂ beam. The ability to engineer phase inhomogeneity and phase transition with strain in VO₂ opens opportunities for designing and controlling functional domains for device and sensor applications. As distinctly different physical and chemical properties are associated with the metallic and insulating phases, interfacing strain-engineered VO₂ with other molecular, nano- or polymeric materials may provide new assembly strategies to achieve collective and externally tunable properties. Recently strain was also employed to manipulate ferroelastic domain patterns in VO₂ nanowires and nano-platelets [187]. Similar approaches can be applied in other TMOs and may lead to new revolutions of strain engineering solid state materials to achieve collective functionalities.

3.2.5. New phase stabilization with strain

The role of the structural transition from the monoclinic to rutile phases during the MIT in VO₂ has been well documented. This monoclinic phase is typically referred to as M1 phase and the rutile phase is R. It is known that strain can complicate the phase transition and induce another monoclinic structure of VO₂, the M2 phase [188]. The structure of M1 phase is characterized by a dimerization of vanadium atoms and a tilt of these pairs with respect to the rutile *c*-axis. In M2 structure, however, only half of the vanadium atoms dimerize while the other half form zigzag chains. M2 structure has been widely observed in Cr-doped samples [170,172,189]. Recent experiments show more evidence that under certain strain state M2 can act as a transitional structure for the phase transition from M1 to the R phase [190–194]. Working on an ensemble of single-crystal VO₂ nanowires with *in situ* synchrotron XRD, it is proposed that surface-stress can induce the M2 phase [190]. The influence of substrate on the production of VO₂ nanoparticles in M1 and M2 phases were also studied [191]. Extensive measurements using infrared scattering–scanning near-field optical microscopy, Raman spectroscopy, and electrical transport have been performed to probe these phases [192–194]. Recently the complicated phase diagram covering all three phases (M1, M2 and rutile) over a wide strain range has been mapped out using VO₂ nanobeams, taking advantage of their superior elastic flexibility [194], as shown in Fig. 16(b). Here the complex stress–temperature phase diagram were determined through a combination of *in situ* optical microscope and SEM [194]. The insulating M1/M2 phases from the metallic R phase can be differentiated by their different optical contrast, and the M1 phase from M2 phase can be differentiated by the twinning caused surface corrugation in the latter (Fig. 16(a)). Through high-resolution optical or SEM imaging at various temperature and different bending states, the critical strain at which the system needs to cross the phase boundary in the stress–temperature phase diagram can be determined. Enabled by the superior mechanical properties of single-crystal beams, the uniaxial stress–temperature phase diagram of VO₂ was expanded more than an order of magnitude wider than that was previously achieved in the bulk [188]. Electrical resistance across the insulating M1 and M2 and metallic R phases was measured over the extensive phase diagram, and the M2 phase was found to be more resistive than the M1 phase by a factor of three. The approach can be applied to other strongly correlated electron materials to explore remote phase space and reveal and engineer new properties.

The different crystal structures of R, M1 and M2 phase make them also distinguishable in micro-XRD (μ XRD) [190]. These three structural phase can also be easily differentiated by Raman scattering through the distinct phonon modes at 608 cm⁻¹ (M1 only), 645 cm⁻¹ (M2 only), and featureless spectrum (metallic R) [192,193]. With increasing temperature, it was found that VO₂ beam initially in M1 phase will convert to M2 phase before the final

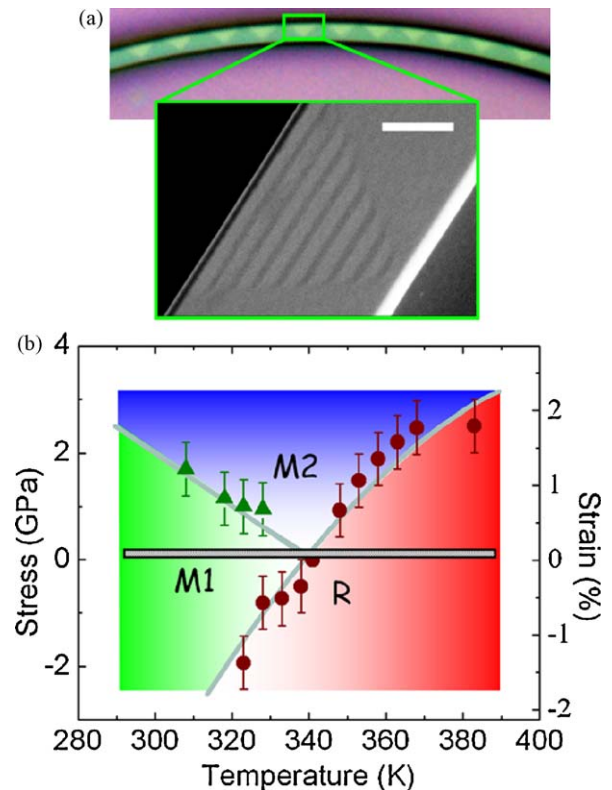


Fig. 16. (a) High-resolution optical and SEM images of a bent VO₂ beam near the natural metal–insulator transition temperature (341 K), showing an array of triangular insulating (bright) and metallic (dark) domains and fine striped structure (M2 phase) within insulating domains. The scale bar is 500 nm. (b) The uniaxial stress–temperature phase diagram of VO₂ obtained by *in situ* optical and SEM imaging of VO₂ beam bending. The lines are guides to the eyes. The rectangular bar area near zero strain is the narrow phase space previously explored in bulk VO₂ [194].

conversion to full metallic phase as: M1 → M1 + R → M2 + R → R. On the other hand, those crystals initially in the M2 phase will transform to R phase directly without passing the M1 phase as: M2 → M2 + R → R [193]. These findings agree well with the proposed stress–temperature phase diagram [194]. By simultaneously performing transport experiments and Raman spectroscopy on the same VO₂ specimen, it is possible to deduce the electrical properties of different phases and associate the structural domain formation with the MIT [192]. The carrier activation energy is reported to be 0.09 eV for M1 phase and 0.43 eV for M2 phase [192]. By direct injection of charge carriers into clamped devices, a metallic monoclinic phase was also reported [192]. This demonstrates that the electrical and structural phase transitions in VO₂ may be decoupled, in which a “true” Mott metal–insulator transition would occur.

4. New opportunities for applications

The strong interactions between spin, lattice, and charge in TMOs make them well suited for investigating a wide variety of properties through their dependence on strain. Strain engineering provides new routes to achieving novel functionalities in advanced materials that can be tailored for many potential applications. Examples include Pb-free ferroelectrics [11,13,105], strain–Mott transistors [173], strain sensors [195], and power generations [165,166], etc. The significant enhancements in Curie temperature and remnant polarization in strained ferroelectrics can be used to replace Pb-based ferroelectrics in potential applications such as ferroelectric random-access memory. Although the effects of strain

on CMR manganite thin films are still controversial, understanding the domain textures and strain-induced magnetic properties is crucial to several technological areas such as magnetic data storage and magnetic sensors. There are many applications for strain engineering in TMO nanowires. Strain-induced domain wall across the metal–insulator transition has been employed to accurately determine the Seebeck coefficient of Schottky junctions [196]. Taking advantage of the spontaneous strain associated with the structural change of the phase transition, a colossal thermal-mechanical actuation in VO₂ microcantilevers was reported, making them suitable for thermal sensors, energy transducers and actuators with unprecedented sensitivities [197]. The introduction of nanopiezotronics should be highlighted here. The basic principle of nanopiezotronics is to use the coupled piezoelectric and semiconducting properties of ZnO nanowires, or other systems that possess these properties, for designing and fabricating devices and components [198]. Many examples such as piezoelectric field-effect transistors, diodes, and humidity sensors have been demonstrated using ZnO nanowires [199–204].

In addition to understanding the properties of existing materials, first-principle calculations have been used to design and discover new materials for future applications. It has been predicted that the strong coupling between spins, optical phonon, and strain can be used to design new multiferroics (simultaneously ferromagnetic and ferroelectric) in strained EuTiO₃ [205]. Although unstrained EuTiO₃ is paraelectric and antiferromagnetic at low temperatures, first-principle calculations indicate that the magnetic (electric) phase control can be achieved by an applied electric (magnetic) field in EuTiO₃ thin films with ~1% biaxial compressive strain. Further, ferroelectrically induced weak ferromagnetism has been predicted in perovskite MnTiO₃ and FeTiO₃ [206]. It is noted that MnTiO₃ and FeTiO₃ have a ground state ilmenite structure. Growing these materials epitaxially on perovskite substrates might be able to stabilize their ground state perovskite structure and to achieve the multiferroic properties in these compounds.

5. Conclusions and outlook

We have presented a comprehensive review of strain effects in TMOs. Engineering strain in TMOs provides a new strategy to probe intrinsic properties and achieve novel functionalities.

Many of the fascinating properties of TMOs originate from the interactions among spin, lattice, and charge degrees of freedom. Lattice strain thus can be used to sensitively tune the electrical, optical, and magnetic properties of these materials. Percent-level strains were applied on coherent epitaxial growth thin films and remarkably different properties have been obtained. They can turn materials that are not ferroelectric at any temperatures into a ferroelectric at room temperature [11]. They can enhance the Curie temperature and remnant electric polarization for better ferroelectrics [13,16]. The effect of strain on phase inhomogeneity and transport properties of CMR manganites have been addressed, although many of the topics still remain open and future experiments are needed to solve these problems. The coupling of electric field and mechanical strain in TMO piezoelectric nanowires provides routes for energy harvesting at small scales and many other potential applications using the piezoelectric effects [43,198]. The unique size and extremely flexible mechanical properties of TMO nanowires offer a platform to investigate intrinsic properties such as phase transition, domain dynamics and domain manipulations [173,175,178,182,193,194]. Theoretical calculations not only yielded extensive and detailed understanding of the experimental observations, but also offered opportunities of designing and discovering new functional materials [205,206].

There is still a long way to go for a full control of strain in TMOs. Improved theoretical models, synthesis techniques and character-

ization tools are needed to provide a comprehensive understanding of the strain effect. There are still many open questions of the strain effect on manganite films, such as the origin of phase inhomogeneity and its effect on transport properties. Systematic investigations, especially *in situ* experiments, are key components to resolving these enigmas. TMO nanowires can sustain an extraordinary amount of uniaxial strain as well as be subjected to continuously tunable external stress, making them suitable for a variety of *in situ* experiments. The availability of TMO nanowires and *in situ* characterization techniques are critical for future strain experiments. Strain engineering of TMOs provides great opportunities for scientific breakthroughs as well as technological innovations that are beneficial to the society.

Acknowledgements

We thank our colleagues and collaborators for sharing their insights on projects related to the topic area, including C. Barrett, K. Chen, L.Q. Chen, E. Ertekin, W. Fan, J.C. Grossman, Y. Gu, S. Huang, D.R. Khanal, M. Kunz, D.F. Ogletree, V. Srinivasan, N. Tamura, Z.L. Wang, J.W.L. Yim, R. Ramesh, E. Saiz, D.G. Schlom, J. Seidel, Q. Yuan, H. Zheng, and R.K. Zheng. We greatly acknowledge the financial support of National Science Foundation under Grant No. EEC-0832819.

References

- [1] P.A. Cox, *Transition Metal Oxides: An Introduction to Their Electronic Structure and Properties*, Oxford University Press, 1992
- [2] N.A. Spaldin, M. Fiebig, *Science* 309 (2005) 391–392.
- [3] E. Dagotto, *Science* 309 (2005) 257–262.
- [4] E.A. Fitzgerald, S.B. Samavedam, Y.H. Xie, L.M. Giovane, J. Vac. Sci. Technol. A 15 (1997) 1048–1056.
- [5] J. Welsler, J.L. Hoyt, J.F. Gibbons, *IEEE Electron Device Lett.* 15 (1994) 100–102.
- [6] A.K. Goswami, L.E. Cross, *Phys. Rev.* 171 (1968) 549.
- [7] G.A. Samara, *Phys. Rev.* 151 (1966) 378.
- [8] I. Bozovic, G. Logvenov, I. Belca, B. Narimbetov, I. Sveklo, *Phys. Rev. Lett.* 89 (2002) 107001.
- [9] H. Sato, M. Naito, *Physica C* 274 (1997) 221–226.
- [10] J.P. Locquet, J. Perret, J. Fompeyrine, E. Machler, J.W. Seo, G. Van Tendeloo, *Nature* 394 (1998) 453–456.
- [11] J.H. Haeni, P. Irvin, W. Chang, R. Uecker, P. Reiche, Y.L. Li, S. Choudhury, W. Tian, M.E. Hawley, B. Craigo, A.K. Tagantsev, X.Q. Pan, S.K. Streiffer, L.Q. Chen, S.W. Kirchoefer, J. Levy, D.G. Schlom, *Nature* 430 (2004) 758–761.
- [12] S.K. Streiffer, J.A. Eastman, D.D. Fong, C. Thompson, A. Munkholm, M.V. Ramana Murty, O. Auciello, G.R. Bai, G.B. Stephenson, *Phys. Rev. Lett.* 89 (2002) 067601.
- [13] K.J. Choi, M. Biegalski, Y.L. Li, A. Sharan, J. Schubert, R. Uecker, P. Reiche, Y.B. Chen, X.Q. Pan, V. Gopalan, L.-Q. Chen, D.G. Schlom, C.B. Eom, *Science* 306 (2004) 1005–1009.
- [14] J. Zhang, H. Tanaka, T. Kanki, J.-H. Choi, T. Kawai, *Phys. Rev. B* 64 (2001) 184404.
- [15] X.J. Chen, S. Soltan, H. Zhang, H.U. Habermeier, *Phys. Rev. B* 65 (2002) 174402.
- [16] J. Wang, J.B. Neaton, H. Zheng, V. Nagarajan, S.B. Ogale, B. Liu, D. Viehland, V. Vaithyanathan, D.G. Schlom, U.V. Waghmare, N.A. Spaldin, K.M. Rabe, M. Wuttig, R. Ramesh, *Science* 299 (2003) 1719–1722.
- [17] S.P. Alpay, I.B. Misirlioglu, V. Nagarajan, R. Ramesh, *Appl. Phys. Lett.* 85 (2004) 2044–2046.
- [18] M.-W. Chu, I. Szafraniak, R. Scholz, C. Harnagea, D. Hesse, M. Alexe, U. Gosele, *Nat. Mater.* 3 (2004) 87–90.
- [19] R. Katiyar, Y. Yuzyuk, *Ferroelectrics* 334 (2006) 211–222.
- [20] K. Seshan, *Handbook of Thin-Film Deposition Processes and Techniques: Principles, Methods Equipment and Applications*, Noyes Publications, 2002.
- [21] D.L. Smith, *Thin-Film Deposition: Principles and Practice*, McGraw-Hill Professional, 1995.
- [22] R.K. Zheng, H.U. Habermeier, H.L.W. Chan, C.L. Choy, H.S. Luo, *Phys. Rev. B* 80 (2009) 104433–104438.
- [23] R. Wordenweber, E. Hollmann, M. Ali, J. Schubert, G. Pickartz, T.K. Lee, J. Eur. Ceram. Soc. 27 (2007) 2899–2902.
- [24] Y.-C. Liang, *Surf. Coat. Technol.* 202 (2008) 5436–5439.
- [25] C. Adamo, X. Ke, H.Q. Wang, H.L. Xin, T. Heeg, M.E. Hawley, W. Zander, J. Schubert, P. Schiffer, D.A. Muller, L. Maritato, D.G. Schlom, *Appl. Phys. Lett.* 95 (2009), 112504–112503.
- [26] Y. Lu, J. Klein, F. Herbstritt, J.B. Philipp, A. Marx, R. Gross, *Phys. Rev. B* 73 (2006) 184406–184407.
- [27] S.J. May, T.S. Santos, A. Bhattacharya, *Phys. Rev. B* 79 (2009), 115127–115126.
- [28] J.S. Horwitz, W. Chang, W. Kim, S.B. Qadri, J.M. Pond, S.W. Kirchoefer, D.B. Chrisey, *J. Electroceram.* 4 (2000) 357–363.
- [29] A.K. Pradhan, D.R. Sahu, B.K. Roul, Y. Feng, *Appl. Phys. Lett.* 81 (2002) 3597–3599.

- [30] F.A. Miranda, C.H. Mueller, F.W.V. Keuls, R.R. Romanofsky, *J. Am. Ceram. Soc.* 91 (2008) 1864–1868.
- [31] M. Veis, S. Visnovsky, P. Lecoeur, A.M. Haghiri-Gosnet, J.P. Renard, P. Beauvillain, W. Prellier, B. Mercey, J. Mistrik, T. Yamaguchi, *J. Phys. D: Appl. Phys.* 42 (2009) 195002.
- [32] W.A. Feil, B.W. Wessels, L.M. Tonge, T.J. Marks, *J. Appl. Phys.* 67 (1990) 3858–3861.
- [33] B.S. Kwak, K. Zhang, E.P. Boyd, A. Erbil, B.J. Wilkens, *J. Appl. Phys.* 69 (1991) 767–772.
- [34] F. Weiss, M. Audier, A. Bartaszyte, D. Bellet, C. Girardot, C. Jimenez, J. Kreisel, S. Pignard, M. Salaun, C. Ternon, *Pure Appl. Chem.* 81 (2009) 1523–1534.
- [35] D.G. Schlom, L.-Q. Chen, C.-B. Eom, K.M. Rabe, S.K. Streiffer, J.-M. Triscone, *Annu. Rev. Mater. Res.* 37 (2007) 589–626.
- [36] J.G. Lu, P. Chang, Z. Fan, *Mater. Sci. Eng. R* 52 (2006) 49–91.
- [37] G. Malandrino, S.T. Finocchiaro, R. Lo Nigro, C. Bongiorno, C. Spinella, I.L. Fragala, *Chem. Mater.* 16 (2004) 5559–5561.
- [38] W.I. Park, D.H. Kim, S.W. Jung, G.-C. Yi, *J. Appl. Phys. Lett.* 80 (2002) 4232–4234.
- [39] F. Liu, P.J. Cao, H.R. Zhang, C.M. Shen, Z. Wang, J.Q. Li, H.J. Gao, *J. Cryst. Growth* 274 (2005) 126–131.
- [40] B.S. Guiton, Q. Gu, A.L. Prieto, M.S. Gudiaksen, H. Park, *J. Am. Chem. Soc.* 127 (2005) 498–499.
- [41] J.I. Sohn, H.J. Joo, A.E. Porter, C.-J. Choi, K. Kim, D.J. Kang, M.E. Welland, *Nano Lett.* 7 (2007) 1570–1574.
- [42] Y.W. Heo, D.P. Norton, L.C. Tien, Y. Kwon, B.S. Kang, F. Ren, S.J. Pearton, J.R. LaRoche, *Mater. Sci. Eng. R* 47 (2004) 1–47.
- [43] Z.L. Wang, *Mater. Sci. Eng. R* 64 (2009) 33–71.
- [44] Y. Mao, S. Banerjee, S.S. Wong, *J. Am. Chem. Soc.* 125 (2003) 15718–15719.
- [45] A.L. Roytburd, *J. Appl. Phys.* 83 (1998) 239–245.
- [46] L.-Q. Chen, *J. Am. Ceram. Soc.* 91 (2008) 1835–1844.
- [47] K.M. Rabe, *Curr. Opin. Solid State Mater. Sci.* 9 (2005) 122–127.
- [48] M. Dawber, K.M. Rabe, J.F. Scott, *Rev. Mod. Phys.* 77 (2005) 1083.
- [49] O. Dieguez, K.M. Rabe, D. Vanderbilt, *Phys. Rev. B* 72 (2005) 144101.
- [50] S.M. Nakhmanson, *Phys. Rev. B* 78 (2008), 064107–064105.
- [51] S. Bin-Omran, I. Ponomareva, L. Bellaiche, *Phys. Rev. B* 77 (2008) 144105–144106.
- [52] B.-K. Lai, I.A. Kornev, L. Bellaiche, G.J. Salamo, *J. Appl. Phys. Lett.* 86 (2005), 132904–132903.
- [53] I. Ponomareva, L. Bellaiche, *Phys. Rev. Lett.* 101 (2008) 197602–197604.
- [54] M. Sepiarsky, S. Tinte, *Physica B: Condens. Matter* 404 (2009) 2730–2732.
- [55] J. Paul, T. Nishimatsu, Y. Kawazoe, U.V. Waghmare, *Phys. Rev. Lett.* 99 (2007) 077601–077604.
- [56] J.X. Zhang, D.G. Schlom, L.Q. Chen, C.B. Eom, *J. Appl. Phys. Lett.* 95 (2009), 122904–122903.
- [57] Z.G. Ban, S.P. Alpay, *J. Appl. Phys.* 91 (2002) 9288–9296.
- [58] V.B. Shirokov, Y.I. Yuzyuk, B. Dkhil, V.V. Lemanov, *Phys. Rev. B* 75 (2007) 224116.
- [59] V.B. Shirokov, Y.I. Yuzyuk, B. Dkhil, V.V. Lemanov, *Phys. Rev. B* 79 (2009) 144118–144119.
- [60] Y.L. Li, S.Y. Hu, Z.K. Liu, L.Q. Chen, *Acta Mater.* 50 (2002) 395–411.
- [61] Y.L. Li, S.Y. Hu, Z.K. Liu, L.Q. Chen, *J. Appl. Phys. Lett.* 78 (2001) 3878–3880.
- [62] O. Dieguez, S. Tinte, A. Antons, C. Bungaro, J.B. Neaton, K.M. Rabe, D. Vanderbilt, *Phys. Rev. B* 69 (2004) 212101.
- [63] Y.L. Li, S. Choudhury, J.H. Haeni, M.D. Biegalski, A. Vasudevarao, A. Sharan, H.Z. Ma, J. Levy, V. Gopalan, S. Trolier-McKinstry, D.G. Schlom, Q.X. Jia, L.Q. Chen, *Phys. Rev. B* 73 (2006) 184112.
- [64] Y.L. Li, L.E. Cross, L.Q. Chen, *J. Appl. Phys.* 98 (2005) 064101–064104.
- [65] D.D. Fong, G.B. Stephenson, S.K. Streiffer, J.A. Eastman, O. Auciello, P.H. Fuoss, C. Thompson, *Science* 304 (2004) 1650–1653.
- [66] D.A. Tenne, A. Bruchhausen, N.D. Lanzillotti-Kimura, A. Fainstein, R.S. Katiyar, A. Cantarero, A. Soukiassian, V. Vaithyanathan, J.H. Haeni, W. Tian, D.G. Schlom, K.J. Choi, D.M. Kim, C.B. Eom, H.P. Sun, X.Q. Pan, Y.L. Li, L.Q. Chen, Q.X. Jia, S.M. Nakhmanson, K.M. Rabe, X.X. Xi, *Science* 313 (2006) 1614–1616.
- [67] H.P. Sun, W. Tian, X.Q. Pan, J.H. Haeni, D.G. Schlom, *J. Appl. Phys. Lett.* 84 (2004) 3298–3300.
- [68] S. Venkatesan, A. Vlooswijk, B.J. Kooi, A. Morelli, G. Palasantzas, J.T.M. De Hosson, B. Noheda, *Phys. Rev. B* 78 (2008) 104112–104118.
- [69] M.D. Biegalski, D.D. Fong, J.A. Eastman, P.H. Fuoss, S.K. Streiffer, T. Heeg, J. Schubert, W. Tian, C.T. Nelson, X.Q. Pan, M.E. Hawley, M. Bernhagen, P. Reiche, R. Uecker, S. Trolier-McKinstry, D.G. Schlom, *J. Appl. Phys.* 104 (2008) 114109–114111.
- [70] C. Lichtensteiger, J.-M. Triscone, J. Junquera, P. Ghosez, *Phys. Rev. Lett.* 94 (2005) 047603.
- [71] D.D. Fong, C. Cionca, Y. Yacoby, G.B. Stephenson, J.A. Eastman, P.H. Fuoss, S.K. Streiffer, C. Thompson, R. Clarke, R. Pindak, E.A. Stern, *Phys. Rev. B* 71 (2005) 144112.
- [72] A. Grigoriev, D.-H. Do, D.M. Kim, C.-B. Eom, B. Adams, E.M. Dufresne, P.G. Evans, *Phys. Rev. Lett.* 96 (2006) 187601–187604.
- [73] C. Thompson, D.D. Fong, R.V. Wang, F. Jiang, S.K. Streiffer, K. Latifi, J.A. Eastman, P.H. Fuoss, G.B. Stephenson, *J. Appl. Phys. Lett.* 93 (2008) 182901–182903.
- [74] R.V. Wang, D.D. Fong, F. Jiang, M.J. Highland, P.H. Fuoss, C. Thompson, A.M. Kolpak, J.A. Eastman, S.K. Streiffer, A.M. Rappe, G.B. Stephenson, *Phys. Rev. Lett.* 102 (2009) 047601–047604.
- [75] L. Despont, C. Koitzsch, F. Clerc, M.G. Garnier, P. Aebi, C. Lichtensteiger, J.M. Triscone, F.J.G. de Abajo, E. Bousquet, P. Ghosez, *Phys. Rev. B* 73 (2006) 094110–094116.
- [76] D.A. Tenne, X. Xi, *J. Am. Ceram. Soc.* 91 (2008) 1820–1834.
- [77] D.A. Tenne, H.N. Lee, R.S. Katiyar, X.X. Xi, *J. Appl. Phys.* 105 (2009), 054106–054105.
- [78] M. El Marssi, F. Le Marrec, I.A. Lukyanchuk, M.G. Karkut, *J. Appl. Phys.* 94 (2003) 3307–3312.
- [79] A. Vasudevarao, S. Denev, M.D. Biegalski, Y. Li, L.-Q. Chen, S. Trolier-McKinstry, D.G. Schlom, V. Gopalan, *J. Appl. Phys. Lett.* 92 (2008) 192902–192903.
- [80] S.V. Kalinin, A. Gruverman, *Scanning Probe Microscopy: Electrical and Electro-mechanical Phenomena at the Nanoscale*, Springer Verlag, 2007.
- [81] P. Shafer, F. Zavaliche, Y.H. Chu, P.L. Yang, M.P. Cruz, R. Ramesh, *J. Appl. Phys. Lett.* 90 (2007), 202909–202903.
- [82] F. Zavaliche, P. Shafer, R. Ramesh, M.P. Cruz, R.R. Das, D.M. Kim, C.B. Eom, *J. Appl. Phys. Lett.* 87 (2005) 252902–252903.
- [83] M. Alexe, A. Gruverman, *Nanoscale Characterisation of Ferroelectric Materials: Scanning Probe Microscopy Approach*, Springer-Verlag, 2004.
- [84] S. Kalinin, A. Kholkin, A. Gruverman, D. Bonnell, *MRS Bull.* 34 (2009) 648657.
- [85] G. Catalan, L.J. Sinnamon, J.M. Gregg, *J. Phys.: Condens. Matter* 16 (2004) 2253–2264.
- [86] G. Sheng, J.X. Zhang, Y.L. Li, S. Choudhury, Q.X. Jia, Z.K. Liu, L.Q. Chen, *J. Appl. Phys.* 104 (2008), 054105–054104.
- [87] J.H. Qiu, Q. Jiang, *J. Appl. Phys.* 101 (2007) 034110–034117.
- [88] J. Wang, T.-Y. Zhang, *J. Appl. Phys. Lett.* 86 (2005), 192905–192903.
- [89] J. Wang, T.-Y. Zhang, *Phys. Rev. B* 77 (2008) 014104–014107.
- [90] V. Nagarajan, S. Prasertchoung, T. Zhao, H. Zheng, J. Ouyang, R. Ramesh, W. Tian, X.Q. Pan, D.M. Kim, C.B. Eom, H. Kohlstedt, R. Waser, *J. Appl. Phys. Lett.* 84 (2004) 5225–5227.
- [91] N. Setter, D. Damjanovic, L. Eng, G. Fox, S. Gevorgian, S. Hong, A. Kingon, H. Kohlstedt, N.Y. Park, G.B. Stephenson, I. Stoltichnov, A.K. Tagantsev, D.V. Taylor, T. Yamada, S. Streiffer, *J. Appl. Phys.* 100 (2006) 051606–051646.
- [92] Y.L. Li, S. Choudhury, Z.K. Liu, L.Q. Chen, *J. Appl. Phys. Lett.* 83 (2003) 1608–1610.
- [93] Z. Wu, N. Huang, J. Wu, W. Duan, B.-L. Gu, *J. Appl. Phys. Lett.* 86 (2005) 202903.
- [94] V. Nagarajan, I.G. Jenkins, S.P. Alpay, H. Li, S. Aggarwal, L. Salamanca-Riba, A.L. Roytburd, R. Ramesh, *J. Appl. Phys.* 86 (1999) 595–602.
- [95] L. Feigl, I.B. Misirlioglu, I. Vrejoiu, M. Alexe, D. Hesse, *J. Appl. Phys.* 105 (2009) 061607.
- [96] Y.L. Li, L.Q. Chen, *J. Appl. Phys. Lett.* 88 (2006), 072905–072903.
- [97] N.A. Pertsev, A.K. Tagantsev, N. Setter, *Phys. Rev. B* 61 (2000) R825.
- [98] M.D. Biegalski, E. Vlahos, G. Sheng, Y.L. Li, M. Bernhagen, P. Reiche, R. Uecker, S.K. Streiffer, L.Q. Chen, V. Gopalan, D.G. Schlom, S. Trolier-McKinstry, *Phys. Rev. B* 79 (2009), 224117–224111.
- [99] C. Ederer, N.A. Spaldin, *Phys. Rev. Lett.* 95 (2005) 257601.
- [100] C. Ederer, N.A. Spaldin, *Phys. Rev. B* 71 (2005) 224103.
- [101] Q. Jiang, J.H. Qiu, *J. Appl. Phys.* 99 (2006) 103901–103906.
- [102] H. Ma, L. Chen, *Comput. Mater. Sci.* 44 (2008) 82–85.
- [103] H. Ma, L. Chen, J. Wang, J. Ma, F. Boey, *J. Appl. Phys. Lett.* 92 (2008) 182902–182903.
- [104] J.X. Zhang, Y.L. Li, Y. Wang, Z.K. Liu, L.Q. Chen, Y.H. Chu, F. Zavaliche, R. Ramesh, *J. Appl. Phys.* 101 (2007) 114105–114106.
- [105] R.J. Zeches, M.D. Rossell, J.X. Zhang, A.J. Hatt, Q. He, C.-H. Yang, A. Kumar, C.H. Wang, A. Melville, C. Adamo, G. Sheng, Y.-H. Chu, J.F. Ihlefeld, R. Erni, C. Ederer, V. Gopalan, L.Q. Chen, D.G. Schlom, N.A. Spaldin, L.W. Martin, R. Ramesh, *Science* 326 (2009) 977–980.
- [106] H.W. Jang, S.H. Baek, D. Ortiz, C.M. Folkman, R.R. Das, Y.H. Chu, P. Shafer, J.X. Zhang, S. Choudhury, V. Vaithyanathan, Y.B. Chen, D.A. Felker, M.D. Biegalski, M.S. Rzhchowski, X.Q. Pan, D.G. Schlom, L.Q. Chen, R. Ramesh, C.B. Eom, *Phys. Rev. Lett.* 101 (2008) 107602–107604.
- [107] J.X. Zhang, Y.L. Li, S. Choudhury, L.Q. Chen, Y.H. Chu, F. Zavaliche, M.P. Cruz, R. Ramesh, Q.X. Jia, *J. Appl. Phys.* 103 (2008) 094111–094116.
- [108] F. Zavaliche, R.R. Das, D.M. Kim, C.B. Eom, S.Y. Yang, P. Shafer, R. Ramesh, *J. Appl. Phys. Lett.* 87 (2005) 182912–182913.
- [109] Y.H. Chu, M.P. Cruz, C.H. Yang, L.W. Martin, P.L. Yang, J.X. Zhang, K. Lee, P. Yu, L.Q. Chen, R. Ramesh, *Adv. Mater.* 19 (2007) 2662–2666.
- [110] Y.H. Chu, Q. Zhan, L.W. Martin, M.P. Cruz, P.L. Yang, G.W. Pabst, F. Zavaliche, S.Y. Yang, J.X. Zhang, L.Q. Chen, D.G. Schlom, I.N. Lin, T.B. Wu, R. Ramesh, *Adv. Mater.* 18 (2006) 2307–2311.
- [111] M.P. Cruz, Y.H. Chu, J.X. Zhang, P.L. Yang, F. Zavaliche, Q. He, P. Shafer, L.Q. Chen, R. Ramesh, *Phys. Rev. Lett.* 99 (2007) 217601–217604.
- [112] M.B. Salamon, M. Jaime, *Rev. Mod. Phys.* 73 (2001) 583–1583.
- [113] A.J. Millis, *Nature* 392 (1998) 147–150.
- [114] A.J. Millis, T. Darling, A. Migliori, *J. Appl. Phys.* 83 (1998) 1588–1591.
- [115] A.J. Millis, P.B. Littlewood, B.I. Shraiman, *Phys. Rev. Lett.* 74 (1995) 5144.
- [116] E. Dagotto, *Nanoscale Phase Separation and Colossal Magnetoresistance*, Springer, 2002.
- [117] J. Burgu, A. Moreo, E. Dagotto, *Phys. Rev. Lett.* 92 (2004) 097202.
- [118] A. Moreo, S. Yunoki, E. Dagotto, *Science* 283 (1999) 2034–2040.
- [119] K.H. Ahn, T. Lookman, A.R. Bishop, *Nature* 428 (2004) 401–404.
- [120] M. Uehara, S. Mori, C.H. Chen, S.W. Cheong, *Nature* 399 (1999) 560–563.
- [121] M. Faeth, S. Freisem, A.A. Menovsky, Y. Tomioka, J. Aarts, J.A. Mydosh, *Science* 285 (1999) 1540–1542.
- [122] C. Renner, G. Aeppli, B.G. Kim, Y.-A. Soh, S.W. Cheong, *Nature* 416 (2002) 518–521.
- [123] L. Zhang, C. Israel, A. Biswas, R.L. Greene, A. de Lozanne, *Science* 298 (2002) 805–807.
- [124] N. Mathur, P. Littlewood, *Phys. Today* 56 (2003) 25.
- [125] J. Schmalian, P.G. Wolynes, *Phys. Rev. Lett.* 85 (2000) 836.
- [126] G.C. Milward, M.J. Calderon, P.B. Littlewood, *Nature* 433 (2005) 607–610.

- [127] T.Z. Ward, J.D. Budai, Z. Gai, J.Z. Tischler, L. Yin, J. Shen, *Nat. Phys.* 5 (2009) 885–888.
- [128] T.-H. Kim, M. Angst, B. Hu, R. Jin, X.G. Zhang, J.F. Wendelken, E.W. Plummer, A.-P. Li, *Proc. Natl. Acad. Sci.* 107 (2010) 5272–5275.
- [129] E. Dagotto, T. Hotta, A. Moreo, *Phys. Rep.* 344 (2001) 1–153.
- [130] M. Angeloni, G. Balestrino, N.G. Boggio, P.G. Medaglia, P. Orgiani, A. Tebano, *J. Appl. Phys.* 96 (2004) 6387–6392.
- [131] G. Ovsyannikov, A. Petrzhiik, I. Borisenko, A. Klimov, Y. Ignatov, V. Demidov, S. Nikitov, *J. Exp. Theor. Phys.* 108 (2009) 48–55.
- [132] F. Tsui, M.C. Smoak, T.K. Nath, C.B. Eom, *Appl. Phys. Lett.* 76 (2000) 2421–2423.
- [133] P. Murugavel, J.H. Lee, J.-G. Yoon, T.W. Noh, J.S. Chung, M. Heu, S. Yoon, *Appl. Phys. Lett.* 82 (2003) 1908–1910.
- [134] J. Dvorak, Y.U. Idzerda, S.B. Ogale, S. Shinde, T. Wu, T. Venkatesan, R. Godfrey, R. Ramesh, *J. Appl. Phys.* 97 (2005) 10C102.
- [135] Y. Lu, J. Klein, C. Hofener, B. Wiedenhorst, J.B. Philipp, F. Herbstritt, A. Marx, L. Alff, R. Gross, *Phys. Rev. B* 62 (2000) 15806.
- [136] M. Kanai, H. Tanaka, T. Kawai, *Phys. Rev. B* 70 (2004) 125109.
- [137] T. Kanki, T. Yanagida, B. Vilquin, H. Tanaka, T. Kawai, *Phys. Rev. B* 71 (2005) 012403.
- [138] H. Tanaka, Y. Takata, K. Horiba, M. Taguchi, A. Chainani, S. Shin, D. Miwa, K. Tamasaku, Y. Nishino, T. Ishikawa, E. Ikenaga, M. Awaji, A. Takeuchi, T. Kawai, K. Kobayashi, *Phys. Rev. B* 73 (2006) 094403–094406.
- [139] Q. Yuan, *Phys. Rev. B* 70 (2004) 066401.
- [140] P. Murugavel, J.H. Lee, K.B. Lee, J.H. Park, J.S. Chung, J.G. Yoon, T.W. Noh, *J. Phys. D: Appl. Phys.* 35 (2002) 3166–3170.
- [141] P. Murugavel, T.W. Noh, J.-G. Yoon, *J. Appl. Phys.* 95 (2004) 2536–2539.
- [142] P. Orgiani, A. Guarino, C. Aruta, C. Adamo, A. Galdi, A.Y. Petrov, R. Savo, L. Maritato, *J. Appl. Phys.* 101 (2007) 033904–033905.
- [143] M. Paranjape, A.K. Raychaudhuri, N.D. Mathur, M.G. Blamire, *Phys. Rev. B* 67 (2003) 214415.
- [144] Y.M. Xiong, G.Y. Wang, X.G. Luo, C.H. Wang, X.H. Chen, X. Chen, C.L. Chen, *J. Appl. Phys.* 97 (2005) 083909–083911.
- [145] Z.Q. Yang, R. Hendrikx, J. Aarts, Y.L. Qin, H.W. Zandbergen, *Phys. Rev. B* 70 (2004) 174111.
- [146] M. Ziese, H.C. Semmelhack, K.H. Han, *Phys. Rev. B* 68 (2003) 134444.
- [147] C. Thiele, K. Dorr, S. Fahler, L. Schultz, D.C. Meyer, A.A. Levin, P. Paufler, *Appl. Phys. Lett.* 87 (2005) 262502–262503.
- [148] C. Thiele, K. Dorr, O. Bilani, J. Rodel, L. Schultz, *Phys. Rev. B* 75 (2007) 054408.
- [149] R.K. Zheng, C. Chao, H.L.W. Chan, C.L. Choy, H.S. Luo, *Phys. Rev. B* 75 (2007) 024110–024116.
- [150] R.K. Zheng, Y. Jjiang, Y. Wang, H.L.W. Chan, C.L. Choy, H.S. Luo, *Phys. Rev. B* 79 (2009) 174420–174427.
- [151] R.K. Zheng, J. Wang, X.Y. Zhou, Y. Wang, H.L.W. Chan, C.L. Choy, H.S. Luo, *J. Appl. Phys.* 99 (2006) 123714–123715.
- [152] R.K. Zheng, Y. Wang, H.L.W. Chan, C.L. Choy, H.S. Luo, *Phys. Rev. B* 75 (2007) 212102–212104.
- [153] R.K. Zheng, Y. Wang, J. Wang, K.S. Wong, H.L.W. Chan, C.L. Choy, H.S. Luo, *Phys. Rev. B* 74 (2006) 094427–094428.
- [154] Z.G. Sheng, J. Gao, Y.P. Sun, *Phys. Rev. B* 79 (2009) 174437–174436.
- [155] M.S. Majdoub, P. Sharma, T. Cagin, *Phys. Rev. B* 78 (2008) 121407–121404.
- [156] M.S. Majdoub, P. Sharma, T. Cagin, *Phys. Rev. B* 77 (2008) 125424–125429.
- [157] L. Cross, *J. Mater. Sci.* 41 (2006) 53–63.
- [158] J.Y. Fu, W. Zhu, N. Li, L.E. Cross, *J. Appl. Phys.* 100 (2006) 024112–024116.
- [159] J.Y. Fu, W. Zhu, N. Li, N.B. Smith, L.E. Cross, *Appl. Phys. Lett.* 91 (2007) 182910–182913.
- [160] W. Ma, L.E. Cross, *Appl. Phys. Lett.* 88 (2006) 232902–232903.
- [161] P. Zubko, G. Catalan, A. Buckley, P.R.L. Welche, J.F. Scott, *Phys. Rev. Lett.* 99 (2007) 167601–167604.
- [162] Z. Wang, J. Hu, A.P. Suryavanshi, K. Yum, M.-F. Yu, *Nano Lett.* 7 (2007) 2966–2969.
- [163] Y. Qin, X. Wang, Z.L. Wang, *Nature* 451 (2008) 809–813.
- [164] Z.L. Wang, *Adv. Funct. Mater.* 18 (2008) 3553–3567.
- [165] Z.L. Wang, J. Song, *Science* 312 (2006) 242–246.
- [166] X. Wang, J. Song, J. Liu, Z.L. Wang, *Science* 316 (2007) 102–105.
- [167] R. Yang, Y. Qin, L. Dai, Z.L. Wang, *Nat. Nanotechnol.* 4 (2009) 34–39.
- [168] R. Yang, Y. Qin, C. Li, G. Zhu, Z.L. Wang, *Nano Lett.* 9 (2009) 1201–1205.
- [169] Y. Gao, Z.L. Wang, *Nano Lett.* 9 (2009) 1103–1110.
- [170] V. Eyert, *Ann. Phys.* 11 (2002) 650–704.
- [171] C.N. Berglund, H.J. Guggenheim, *Phys. Rev.* 185 (1969) 1022–1033.
- [172] M. Marezio, D.B. McWhan, J.P. Remeika, P.D. Dernier, *Phys. Rev. B* 5 (1972) 2541–2551.
- [173] J. Cao, E. Ertekin, V. Srinivasan, W. Fan, S. Huang, H. Zheng, J.W.L. Yim, D.R. Khanal, D.F. Ogletree, J.C. Grossman, J. Wu, *Nat. Nanotechnol.* 4 (2009) 732–737.
- [174] M.M. Qazilbash, M. Brehm, B.-G. Chae, P.-C. Ho, G.O. Andreev, B.-J. Kim, S.J. Yun, A.V. Balatsky, M.B. Maple, F. Keilmann, H.-T. Kim, D.N. Basov, *Science* 318 (2007) 1750–1753.
- [175] J. Wu, Q. Gu, B.S. Guiton, N.P. de Leon, L. Ouyang, H. Park, *Nano Lett.* 6 (2006) 2313–2317.
- [176] W.-T. Liu, J. C. Cao, W. Fan, H. Zhao, M. C. Martin, J. Wu, F. Wang, submitted for publication.
- [177] D. Natelson, *Nat. Nanotechnol.* 4 (2009) 406–407.
- [178] J. Wei, Z. Wang, W. Chen, D.H. Cobden, *Nat. Nanotechnol.* 4 (2009) 420–424.
- [179] R.M. Wentzcovitch, W.W. Schulz, P.B. Allen, *Phys. Rev. Lett.* 72 (1994) 3389–3392.
- [180] T.M. Rice, H. Launois, J.P. Pouget, *Phys. Rev. Lett.* 73 (1994) 3042.
- [181] A. Cavalleri, T. Dekorsy, H.H.W. Chong, J.C. Kieffer, R.W. Schoenlein, *Phys. Rev. B* 70 (2004) 161102.
- [182] J. Cao, W. Fan, K. Chen, N. Tamura, M. Kunz, V. Eyert, J. Wu, submitted for publication.
- [183] K. Otsuka, C. Wayman, *Shape Memory Materials*, Cambridge University Press, New York, 1999.
- [184] W. Fan, S. Huang, J. Cao, E. Ertekin, C. Barrett, D.R. Khanal, J.C. Grossman, J. Wu, *Phys. Rev. B* 80 (2009) 241105(R).
- [185] D.A. McQuarrie, J.D. Simon, *Physical Chemistry: A Molecular Approach*, University Science Books, Sausalito, 1997.
- [186] Q. Gu, A. Falk, J. Wu, L. Ouyang, H. Park, *Nano Lett.* 7 (2007) 363–366.
- [187] A. Tselev, E. Strelcov, I.A. Luk'yanchuk, J.D. Budai, J.Z. Tischler, I.N. Ivanov, K. Jones, R. Proksch, S.V. Kalinin, A. Kolmakov, *Nano Lett.* 10 (2010) 2003–2011.
- [188] J.P. Pouget, H. Launois, J.P. D'Haenens, P. Merenda, T.M. Rice, *Phys. Rev. Lett.* 35 (1975) 873–875.
- [189] J.P. Pouget, H. Launois, T.M. Rice, P. Dernier, A. Gossard, G. Villeneuve, P. Hagenmuller, *Phys. Rev. B* 10 (1974) 1801–1815.
- [190] J.I. Sohn, H.J. Joo, D. Ahn, H.H. Lee, A.E. Porter, K. Kim, D.J. Kang, M.E. Welland, *Nano Lett.* 9 (2009) 3392–3397.
- [191] J.M. Booth, P.S. Casey, *ACS Appl. Mater. Interfaces* 1 (2009) 1899–1905.
- [192] S. Zhang, J.Y. Chou, L.J. Lauhon, *Nano Lett.* 9 (2009) 4527–4532.
- [193] A. Jones, S. Berweger, J. Wei, D. Cobden, M. Raschke, *Nano Lett.* 10 (2010) 1574–1581.
- [194] J. Cao, Y. Gu, W. Fan, L.Q. Chen, D.F. Ogletree, K. Chen, N. Tamura, M. Kunz, C. Barrett, J. Seidel, J. Wu, *Nano Lett.* 10 (2010) 2667–2673.
- [195] J. Zhou, Y. Gu, P. Fei, W. Mai, Y. Gao, R. Yang, G. Bao, Z.L. Wang, *Nano Lett.* 8 (2008) 3035–3040.
- [196] J. Cao, W. Fan, H. Zheng, J. Wu, *Nano Lett.* 9 (2009) 4001–4006.
- [197] J. Cao, W. Fan, Q. Zhou, E. Sheu, A. Liu, C. Barrett, J. Wu, submitted for publication.
- [198] Z.L. Wang, *Adv. Mater.* 19 (2007) 889–892.
- [199] J. Zhou, P. Fei, Y. Gu, W. Mai, Y. Gao, R. Yang, G. Bao, Z.L. Wang, *Nano Lett.* 8 (2008) 3973–3977.
- [200] J. Zhou, P. Fei, Y. Gao, Y. Gu, J. Liu, G. Bao, Z.L. Wang, *Nano Lett.* 8 (2008) 2725–2730.
- [201] X. Wang, J. Zhou, J. Song, J. Liu, N. Xu, Z.L. Wang, *Nano Lett.* 6 (2006) 2768–2772.
- [202] J.H. He, C.L. Hsin, J. Liu, L.J. Chen, Z.L. Wang, *Adv. Mater.* 19 (2007) 781–784.
- [203] C.S. Lao, Q. Kuang, Z.L. Wang, M.-C. Park, Y. Deng, *Appl. Phys. Lett.* 90 (2007) 262107–262103.
- [204] T.-Y. Wei, P.-H. Yeh, S.-Y. Lu, Z.L. Wang, *J. Am. Chem. Soc.* 131 (2009) 17690–17695.
- [205] C.J. Fennie, K.M. Rabe, *Phys. Rev. Lett.* 97 (2006) 267602.
- [206] C.J. Fennie, *Phys. Rev. Lett.* 100 (2008) 167203–167204.